A Climatological Analysis of Tropical Cyclone Rapid Intensification in Environments of Upper-Tropospheric Troughs

MICHAEL S. FISCHER, BRIAN H. TANG, AND KRISTEN L. CORBOSIERO

Department of Atmospheric and Environmental Sciences, University at Albany, State University of New York, Albany, New York

ABSTRACT

Tropical cyclone (TC)–trough interactions are a common occurrence in the North Atlantic basin and lead to a variety of TC intensity changes, from rapid intensification (RI) to rapid weakening. To test whether certain TC–trough configurations are more favorable for RI than others, the upper-tropospheric troughs involved in such interactions were objectively classified into one of three clusters through the implementation of a machine-learning, dimensionality-reduction technique in conjunction with a k-means clustering algorithm. Through composite analyses, the upper-tropospheric potential vorticity structure, the TC convective structure, and the TC environment were examined for both rapidly intensifying TCs and nonrapidly intensifying (non-RI) TCs. As a whole, RI episodes were associated with upper-tropospheric troughs of shorter zonal wavelengths and greater upstream TC–trough displacements than non-RI episodes. RI was found to occur most frequently when an upper-tropospheric cutoff low was located approximately 500–1000 km southwest of the TC location. RI occurred preferentially in environments associated with less ventilation of the TC warm core with low-entropy environmental air. An examination of potential trough-induced forcing for convection revealed little relationship between RI and eddy flux convergence of angular momentum. Nonetheless, RI episodes were associated with anomalously vigorous convective activity within the TC inner core, as diagnosed by infrared and passive microwave satellite imagery.

1. Introduction

The rate of tropical cyclone (TC) intensification is dependent upon the interaction of convective-scale processes with the surrounding synoptic-scale environment. Considering the complexities involved in such multiscale interactions, improvements in TC intensity prediction have been challenging. Although operational TC intensity forecasts have experienced gradual improvements over recent years (e.g., DeMaria et al. 2014), TC intensity prediction remains especially challenging during events of TC rapid intensification (RI; Elsberry et al. 2007; Sampson et al. 2011; Kaplan et al. 2015; Emanuel and Zhang 2016). As seen in Fig. 1, operational, 24-h TC intensity forecasts for RI episodes [those with 24-h TC intensification rates of at least 25 kt $(1 \, \mathrm{kt} \approx 0.5144 \, \mathrm{m \, s^{-1}})$] in the North Atlantic basin are associated with significantly larger errors than non-RI

episodes over the last 20–30 years. Additionally, the trend lines in Fig. 1 indicate only small improvements in these forecasts due, in part, to the complexities arising from the multiscale nature of RI. Compounding these issues, TCs that rapidly intensify can be particularly dangerous and costly, as research has shown damages associated with TC landfalls display a power-law dependence on the maximum, sustained 10-m wind speed (Pielke 2007). Accordingly, the National Hurricane Center has made the accurate prediction of episodes of RI one of its top forecast priorities (Rappaport et al. 2012).

Previous work has shown the likelihood of a TC to undergo RI is strongly linked to the prevailing environmental conditions (Kaplan and DeMaria 2003; Kaplan et al. 2010; Rozoff and Kossin 2011; Kaplan et al. 2015; Rozoff et al. 2015). Specifically, RI events are more likely to occur in environments characterized by weak vertical wind shear, a moist troposphere, high oceanic heat content, and upper-tropospheric divergence (Kaplan and DeMaria 2003; Kaplan et al. 2010;

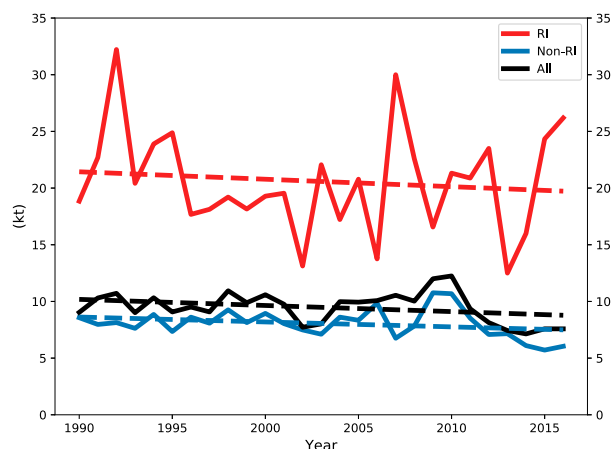*Corresponding author*: Michael S. Fischer, michael.fischer@noaa.gov

FIG. 1. Time series of operational, mean absolute intensity error (kt) from forecasts issued by the National Hurricane Center (NHC) for overwater 24-h intensity forecasts for TCs in the North Atlantic basin from 1990 to 2016. Error is shown for RI episodes (red), non-RI episodes (blue), and all intensity change episodes (black). RI episodes are defined as those with a 24-h change in maximum sustained 10-m winds $\geq$ 25 kt. Linear trends are indicated by the dashed lines.

Rozoff and Kossin 2011; Tang and Emanuel 2012; Kaplan et al. 2015; Rozoff et al. 2015). Case studies of RI events have also linked other environmental influences to increased rates of TC intensification, such as the presence of a nearby upper-tropospheric trough (Molinari and Vollaro 1989; Molinari et al. 1995, 1998; Bosart et al. 2000; Leroux et al. 2013; Shieh et al. 2013; Chen et al. 2015). Such TC–trough interaction events feature notoriously challenging TC intensity forecasts, as the presence of an upper-tropospheric trough can provide unique forcing for convection and TC intensification (e.g., Molinari and Vollaro 1989; Bosart et al. 2000; Fischer et al. 2017); however, troughs are also often associated with unfavorable environmental conditions, such as increased vertical wind shear (Hanley et al. 2001) and dry air (Zhang et al. 2016).

One potential pathway by which an upper-tropospheric trough can induce TC intensification involves an upper-tropospheric trough acting as a source of angular momentum in the TC outflow layer. The convergence of eddy fluxes of angular momentum can enhance the TC secondary circulation, whereby stronger upper-tropospheric outflow favors rising motion in the inner core, greater convective activity, and TC intensification (Pfeffer and Challa 1981; Molinari and Vollaro 1989, 1990). In another proposed pathway, potential vorticity (PV) associated with the trough can be advected inward, underneath the TC outflow layer, in certain TC–trough configurations, and has been hypothesized to enhance the inner-core PV and strengthen

the TC (Leroux et al. 2013, 2016). Other studies have argued upper-tropospheric troughs may invigorate TC convective activity either through quasigeostrophic (QG) forcing for ascent (Bracken and Bosart 2000; Fischer et al. 2017) or through upper-tropospheric jet dynamics (Rodgers et al. 1991; Shi et al. 1997; Bosart et al. 2000; Komaromi and Doyle 2018).

Despite these potential TC intensification mechanisms, prior climatological studies of TC–trough interactions have concluded upper-tropospheric troughs are generally unfavorable for TC intensification (DeMaria et al. 1993; Hanley et al. 2001; Peirano et al. 2018). Nonetheless, since multiple TCs have been documented to undergo RI while interacting with an upper-tropospheric trough, a lingering question is whether certain TC–trough configurations are more favorable for TC RI than others. Furthermore, do the environmental favorability and the trough-induced forcings for convection vary depending on the TC–trough configuration? This study seeks to address the ''good trough/bad trough'' quandary by answering the aforementioned questions.

Prior climatological studies of TC–trough interactions have neglected to examine the relationship between TC intensity change and TC convective characteristics. Considering previous work has shown the rate of TC intensification is closely linked to TC convective structure (e.g., Zagrodnik and Jiang 2014; Alvey et al. 2015; Tao and Jiang 2015; Fischer et al. 2018), the present study seeks to bridge this gap in the literature. Idealized numerical modeling simulations have, in general, demonstrated that a symmetric distribution of diabatic heating is an efficient configuration for TC intensification (Nolan and Grasso 2003; Nolan et al. 2007). These findings are consistent with observational studies that have linked a greater azimuthal coverage of convection, especially in the upshear quadrants of the TC, to greater rates of TC intensification, including rapid intensification (Harnos and Nesbitt 2011, 2016; Kieper and Jiang 2012; Rogers et al. 2013; Zagrodnik and Jiang 2014; Alvey et al. 2015; Kaplan et al. 2015; Tao and Jiang 2015; Rios-Berrios and Torn 2017; Tao et al. 2017).

It is well known from prior work, however, that the azimuthal distribution of convection in a TC is heavily influenced by the direction and magnitude of the vertical wind shear (Corbosiero and Molinari 2002, 2003; Chen et al. 2006; Reasor et al. 2013; DeHart et al. 2014). Typically, as air parcels orbit cyclonically about the TC center, updrafts initiate in the downshear-right quadrant, mature in the downshear-left quadrant, and decay in the upshear quadrants of the TC (Jones 1995; Black et al. 2002; DeHart et al. 2014). Because prior climatologies of TC–trough interactions have found

upper-tropospheric troughs tend to be associated with greater vertical wind shear than environments devoid of troughs (e.g., Hanley et al. 2001), this study also seeks to gain a better understanding of the relationship between trough morphology, vertical wind shear, and TC convective structure.

With these goals in mind, the remainder of this paper is organized as follows: The methods and datasets used in the present analysis are described in section 2. Section 3 will demonstrate how a machine-learning, dimensionality-reduction technique can be utilized to objectively identify three unique TC–trough configurations. Results from the clustering analysis, as well as comparisons of RI and nonrapidly intensifying TCs within each cluster, will be discussed in sections 4–8. Finally, a discussion and summary of the results are provided in section 9.

2. Data and methods

a. Datasets

This study examined tropical and subtropical cyclones that formed in the North Atlantic basin from 1989 to 2016. For simplicity, the remainder of this study will use "TC" to indicate both tropical and subtropical cyclones. TC position and intensity estimates were obtained from the National Hurricane Center best track database (HURDAT2; Landsea and Franklin 2013). Overland TC times, as well as TC times featuring a landfall or extratropical transition within the 24 h following a given best track entry were removed from this analysis. Additionally, TCs located within environments that had a maximum potential intensity (MPI) $<40\,\mathrm{m\,s^{-1}}$ were also excluded. TCs in such environments were found to be less likely to intensify due to unfavorable thermodynamic conditions (e.g., lower sea surface temperatures and drier environments) and are also more likely to be undergoing extratropical transition (Hart and Evans 2001). The MPI was calculated following the methods of Bister and Emanuel (2002) using fields from the European Centre for Medium-Range Weather Forecasts interim reanalysis (ERA-Interim), after masking out potential warm-core temperature anomalies associated with the TC vortex (Dee et al. 2011).

This study frequently employs storm-centered composite analyses. To compute the composites, storm centers were determined using the 850-hPa relative vorticity centroid, computed within a $3° \times 3°$ box centered on the best track location. This "recentering" process corrects for instances when the reanalysis center does not precisely match the best track center location,

potentially due to the relatively coarse resolution of the reanalysis (approximately $0.7° \times 0.7°$).

To analyze TC convective characteristics, this study utilized both infrared (IR) and passive microwave satellite imagery. Infrared brightness temperatures were taken from the GridSat dataset (Knapp et al. 2011), which has a spatial resolution of approximately 10 km × 10 km, with data available every three hours. Microwave brightness temperatures were obtained from the dataset constructed by Fischer et al. (2018), which uses data gathered from six low-Earth-orbiting satellites: the Advanced Microwave Scanning Radiometer for Earth Observing System (AMSR-E), the Advanced Microwave Scanning Radiometer 2 (AMSR-2), the Special Sensor Microwave Imager (SSM/I), the Special Sensor Microwave Imager/Sounder (SSMIS), the Tropical Rainfall Measuring Mission Microwave Imager (TMI), and the Global Precipitation Measurement Microwave Imager (GMI). As in Fischer et al. (2018), the microwave brightness temperatures taken from the six sensors were calibrated to common 37- and 85-GHz frequencies, using a histogram matching technique, similar to Jones and Cecil (2006) and Rozoff et al. (2015). Passive microwave imagery has the benefit of observing the structure of hydrometeors underneath the TC cirrus canopy, unlike IR imagery, but can be limited by intermittent temporal coverage due to the nature of the low-Earth orbit of the satellites. A more detailed explanation of the construction of the microwave dataset can be found in Fischer et al. (2018).

b. Environmental classification and intensity change groups

TCs were classified as occurring in one of three environmental regimes based on the distribution of the maximum PV anomaly magnitude on the 350-K isentropic surface within a 250–1000-km storm-centered annulus ($\mathrm{PV_{max}}$; Fig. 2). The 350-K isentropic surface was selected as previous work has shown it resides near the subtropical tropopause (Postel and Hitchman 1999; Wernli and Sprenger 2007). Using a domain that extends radially outward to 1000 km is consistent with previous TC–trough interaction studies, such as Hanley et al. (2001), although the 1000-km radial limit is smaller than the 1500-km limit used by DeMaria et al. (1993). TCs were classified in either a low-PV environment if $\mathrm{PV_{max}} < 1.0\,\mathrm{PVU}$ ($1\,\mathrm{PVU} = 10^{-6}\,\mathrm{K\,kg^{-1}\,m^2\,s^{-1}}$), a mid-PV environment if $1.0 \le \mathrm{PV_{max}} < 2.0\,\mathrm{PVU}$, or a high-PV environment if $\mathrm{PV_{max}} \ge 2.0\,\mathrm{PVU}$. These groups correspond to approximately the lower, middle, and upper terciles of the distribution, respectively. TCs in high-PV environments were found to be consistently interacting with synoptic-scale upper-tropospheric PV anomalies
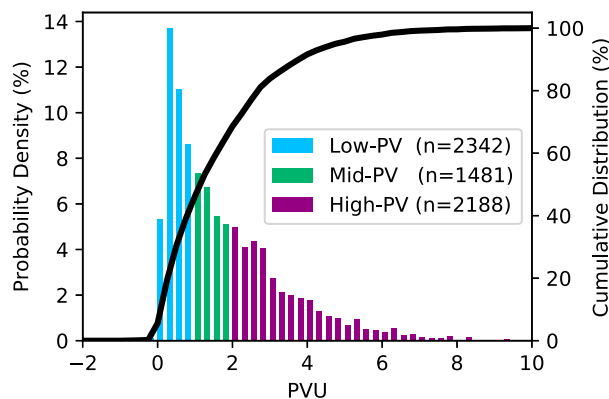
FIG. 2. Distribution of the maximum PV anomaly (PVU) on the 350-K isentropic surface within a 250–1000-km TC-centered annulus for TCs in the North Atlantic basin from 1989 to 2016 in environments characterized by a maximum potential intensity of at least $40 \, \mathrm{m \, s^{-1}}$. The normalized histogram (%; binned every 0.25 PVU) is given by the bars, while the cumulative distribution (%) is represented by the black line. TCs in low-PV, mid-PV, and high-PV environments are represented by blue, green, and purple bars, respectively. The number (n) of TC times in each group is given in the legend.
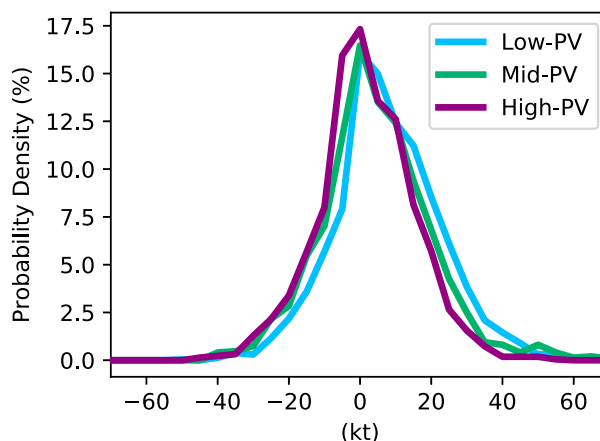

FIG. 3. Normalized histogram (%) of 24-h intensity change (kt) for all overwater TCs in the North Atlantic basin from 1989 to 2016 in environments characterized by a maximum potential intensity of at least $40 \, \mathrm{m \, s^{-1}}$. The intensity change distributions are grouped by the TC environmental classification, where TCs in low-PV, mid-PV, and high-PV environments are represented by blue, green, and purple lines, respectively. The bin interval is 5 kt.

and, as a result, will be used to define TC–trough interactions for the remainder of this analysis. It is possible, if not likely, other methods of identifying TC–trough interactions would provide similar results; however, since the point-based method used here consistently identified synoptic-scale features, it is not believed the results of this analysis are overly sensitive to the trough identification methodology.

Of the three environmental groups, Fig. 3 shows high-PV environments are associated with the smallest rates of TC intensification, as determined by the 24-h change in the maximum sustained 10-m wind speed. In fact, the differences between the three intensity change distributions are all statistically significant at the 99.9% level using the nonparametric, two-tailed Wilcoxon rank-sum test (Wilks 2011). Hereafter, any reference to statistical significance will assume significance of at least the 95% level using the aforementioned Wilcoxon rank-sum test on independent samples. The differences in TC intensity change between the environmental regimes are especially pronounced in the upper tails of the distributions. For example, following the Kaplan and DeMaria (2003) criterion for RI, which is equal to the 95th percentile of the TC intensity change distribution, the threshold for RI differs depending on the environmental regime. Specifically, the RI thresholds for high-PV, mid-PV, and low-PV environments are 25, 30, and 35 kt, respectively. This suggests the presence of an upper-tropospheric PV anomaly is not favorable for, although does not preclude, more rapid rates of

TC intensification, which is consistent with the findings of Hanley et al. (2001).

To determine whether high-PV RI episodes—defined as high-PV TCs with a subsequent 24-h change in the maximum sustained 10-m wind ≥ 25 kt—are associated with unique upper-tropospheric trough morphologies, this study will compare RI episodes to those that do not meet the RI criterion, hereafter referred to as non-RI episodes.

3. Identification of similar TC–trough configurations

The morphologies of upper-tropospheric troughs that interact with TCs display a large amount of variability. Consequently, a composite analysis of all TC–trough interactions yields limited insight. To remedy this issue, similar TC–trough interactions were objectively identified using two different dimensionality-reduction techniques. These techniques facilitate an analysis of whether certain TC–trough configurations are more favorable for RI.

The first dimensionality-reduction technique employed within this analysis was t-distributed stochastic neighbor embedding (t-SNE; Maaten and Hinton 2008; Maaten 2014). Broadly speaking, t-SNE is a member of a larger family of embedding techniques, which allow for the visualization of a high-dimensional dataset within a low-dimensional (e.g., two-dimensional) space. This reduction is accomplished by calculating a similarity matrix in both the high- and low-dimensional

space, yielding a similarity probability distribution for the analyzed object pairs. Ultimately, the visualization resulting from the technique consists of relatively similar objects located closer together within the low-dimensional space and dissimilar objects located farther away, effectively preserving the local data structure, including nonlinear relationships. t-SNE has been utilized as a visualization tool by a number of previous studies, ranging from the identification of extreme weather events in large-scale climate simulations (Racah et al. 2017), to genetic analyses of the human body (Wilson et al. 2015), to the development of a novel artificial agent capable of outplaying humans at multiple video games (Mnih et al. 2015).

The second dimensionality-reduction technique utilized in this study was principal component analysis (PCA), which has been employed more frequently in the atmospheric sciences (e.g., Overland and Preisendorfer 1982; Kossin et al. 2007; Kaplan et al. 2015; Knaff et al. 2015). Unlike t-SNE, PCA operates under the assumption that the identified principal components are orthogonal to each other and therefore attempts to highlight the variance within a given dataset, rather than the similarities.

Both dimensionality-reduction techniques ingested the same input: PV anomalies on the 350-K isentropic surface within a 2000 km $\times$ 2000 km TC-centered box, linearly interpolated to 50 km $\times$ 50 km grid spacing, at every synoptic time, for qualifying high-PV TCs. PV anomalies were calculated relative to a 30-day mean base state, centered on the analysis time. Before the PV anomalies were input into the t-SNE algorithm, PV anomalies at each grid point were rescaled using a minimum–maximum normalization. An example of the low-dimensional representation of each technique is shown in the form of a scatterplot in Figs. 4a and 4b, where each point represents a unique TC–trough interaction episode. Of the two dimensionality-reduction techniques, the t-SNE visualization (Fig. 4a) is characterized by greater local structure, with points primarily contained within three lobes of increased density.

Once the dimensionality-reduction techniques were employed, similar TC–trough configurations were objectively identified using a k-means clustering technique on the low-dimensional visualizations. Since k-means clustering requires the number of clusters to be specified a priori, this study analyzed a range of total clusters. To determine which number of clusters best fit the two-dimensional visualizations in Figs. 4a and 4b, the number of clusters that maximized the silhouette score (e.g., Rousseeuw 1987) was selected. The silhouette score is a measure of cluster cohesiveness and is defined as

$$S = \frac{b - a}{\max(a, b)}, \tag{1}$$

where a is the mean intracluster distance and b is the mean nearest-cluster distance for each sample. The silhouette score is bounded between -1 and 1, with values closer to 1 indicative of greater cluster cohesiveness. Because t-SNE visualizations involve a stochastic component, repeated visualizations of the same dataset can yield slightly different low-dimensional representations. As such, it is possible—although not necessarily likely—one t-SNE visualization yields a maximum silhouette score for a total of three clusters, while another t-SNE visualization yields a maximum silhouette score for a total of seven clusters. To account for this variability, the t-SNE visualization and the ensuing k-means clustering calculation were computed 240 times for $k = 2$–9. The maximum silhouette scores resulting from k-means clustering of the low-dimensional visualizations are provided in Table 1.

From Table 1, it can be seen that employing k-means clustering on the t-SNE visualizations consistently resulted in larger silhouette scores, indicative of greater cluster cohesiveness, than the visualization obtained from PCA. Interestingly, for both t-SNE and PCA, selecting a total of three clusters resulted in the largest silhouette score (Table 1). The $k = 3$ clustering results for both t-SNE and PCA are shown in Figs. 4c and 4d. The more pronounced local structure of the $k = 3$ t-SNE visualization (Fig. 4c), compared to the $k = 3$ PCA visualization (Fig. 4d), is consistent with the larger silhouette score seen in Table 1.

For each cluster, the corresponding storm-centered, composite-mean, PV anomalies on the 350-K isentropic surface are shown in Fig. 5. For a given dimensionality-reduction technique, each composite cluster is associated with a unique TC–trough configuration. The characteristics of certain clusters display a degree of similarity regardless of the dimensionality-reduction technique employed. More specifically, the first two clusters resulting from both t-SNE and PCA yield similar upper-tropospheric PV anomaly morphologies. Cluster-1 TCs are characterized by an upper-tropospheric positive-PV anomaly located directly over, and immediately to the southwest of, the TC, with an upper-tropospheric ridge located to the north of the TC (Figs. 5a,d). Cluster-1 TCs resulting from PCA are associated with a greater extension of the positive-PV anomaly to the northeast of the TC location than cluster-1 TCs using t-SNE, which more closely resembles a cutoff upper-tropospheric cyclone. Cluster-2 TCs are characterized by a prominent, positively tilted, positive upper-tropospheric PV anomaly located to the northwest of the TC, and a negative
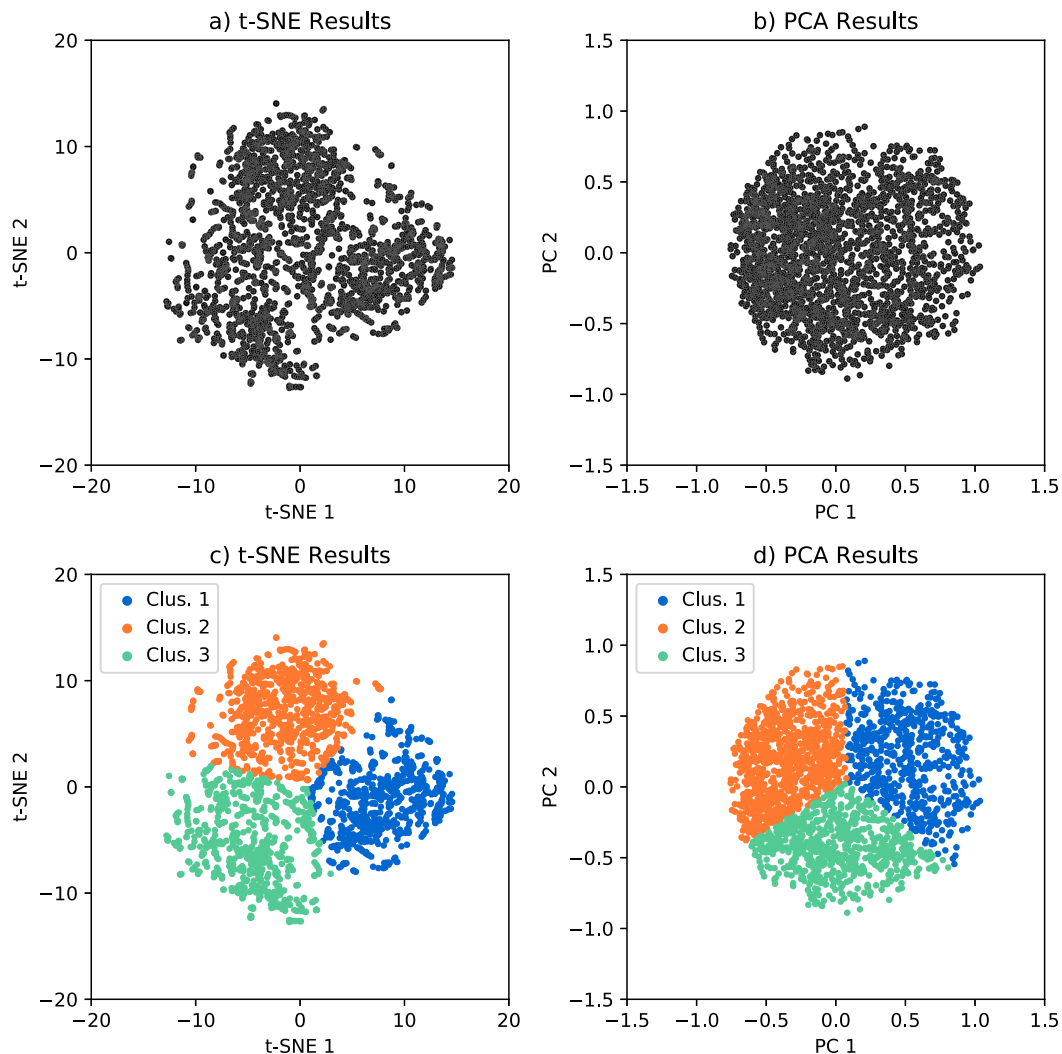
FIG. 4. Scatterplots of the two-dimensional representation of 350-K PV anomalies within a 2000 km × 2000 km TC-centered box using (a) t-SNE and (b) principal component analysis. The units of the axes are dimensionless. (c),(d) As in (a),(b), but the results are grouped by a k-means clustering algorithm, with three clusters.

upper-tropospheric PV anomaly centered northeast of the TC (Figs. 5b,e).

The similarities between the composite clusters using t-SNE and PCA are no longer evident in the final cluster of TC–trough configurations (cluster 3; Figs. 5c and 5f). The composite of cluster-3 TCs resulting from t-SNE is characterized by a positively tilted, positive-PV anomaly maximized northeast of the TC, with a weaker extension trailing toward the southwest, terminating approximately 1000 km west of the TC location (Fig. 5c). Additionally, two separate regions of negative-PV anomalies are observed, with one located directly over, and to the east of, the TC, and a secondary, negative-PV anomaly located approximately 1000–2000 km northwest of the TC (Fig. 5c). In comparison, the composite of cluster-3 TCs resulting from PCA is devoid of

positive-PV anomalies > 0.5 PVU (Fig. 5f). Instead, a large negative-PV anomaly is observed directly over, and to the north of, the TC location (Fig. 5f).

Since the composites shown in Fig. 5 require TCs to be within 1000 km of a positive-PV anomaly of a magnitude of at least 2.0 PVU (Fig. 2), it is likely the locations of

TABLE 1. Silhouette scores of k-means clustering on t-distributed stochastic neighbor embedding (t-SNE) and principal component analysis (PCA) dimensionality reduction results of 350-K PV anomalies within a 2000 km × 2000 km TC-centered box, grouped by the number of k-means clusters.

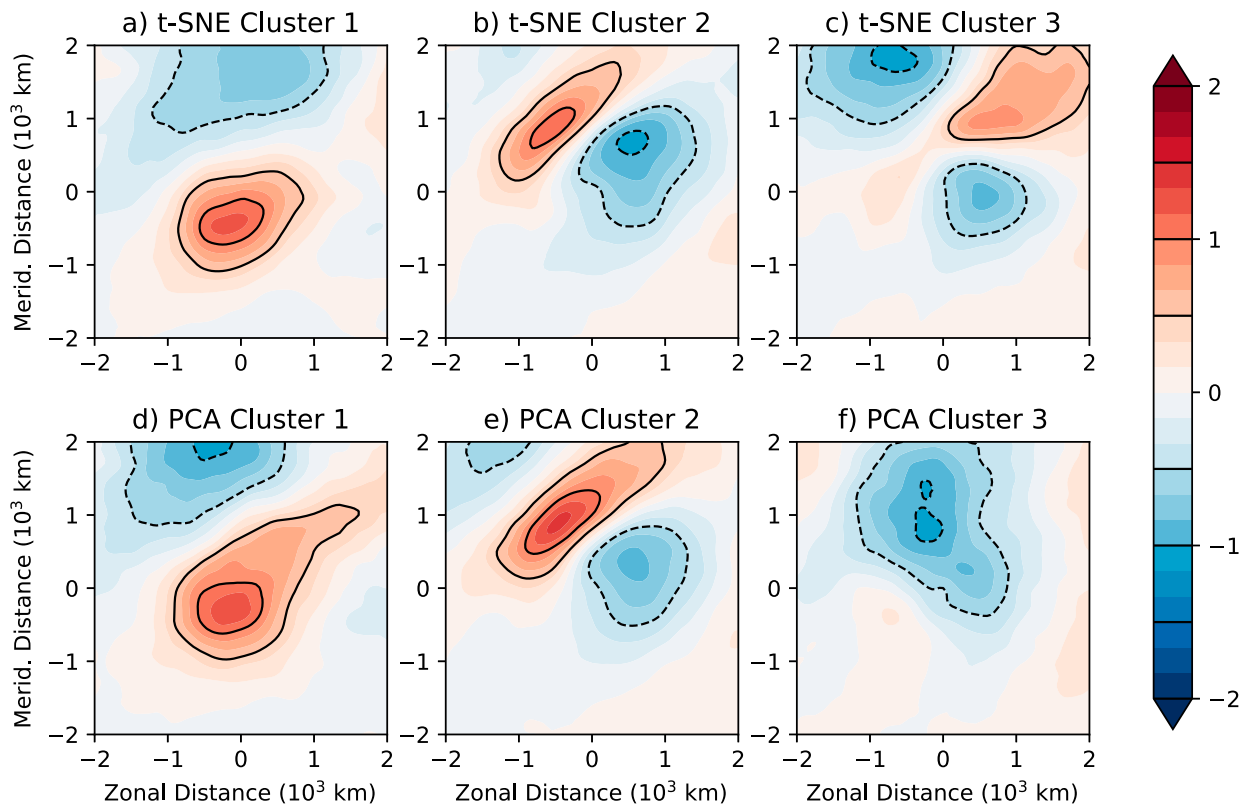| Technique	2	3	4	5	6	7	8
t-SNE	0.44	0.47	0.44	0.44	0.44	0.42	0.41
PCA	0.39	0.39	0.38	0.36	0.36	0.37	0.36

FIG. 5. Composite-mean, storm-centered, PV anomalies (PVU; shaded, with black contours drawn every 0.5 PVU) on the 350-K isentropic surface for high-PV TCs in the North Atlantic basin. TCs are grouped by the clustered results shown in Fig. 4, using k-means clustering in conjunction with (a)–(c) t-distributed stochastic neighbor embedding and (d)–(f) principal component analysis. The zonal and meridional distance (10^3 km) from the TC center is displayed along the abscissa and ordinate of each plot, respectively.

the positive-PV anomalies associated with PCA cluster-3 TCs are scattered about the domain, resulting in a muted, positive-PV anomaly signal upon averaging the cluster members. Thus, in this application, t-SNE is better at identifying relatively similar, coherent TC–trough configurations than PCA. Furthermore, since the $k = 3$ clustering of the t-SNE visualization yielded the largest silhouette score, the remainder of this analysis will focus on the three TC–trough configurations resulting from t-SNE. For simplicity, the three TC–trough configuration clusters obtained via t-SNE will hereafter be referred to as the cutoff cluster (cluster 1), the northwest (NW) trough cluster (cluster 2), and the northeast (NE) trough cluster (cluster 3), in reference to the trough morphology of each cluster (Figs. 5a–c).

4. Climatological TC characteristics of three TC–trough interaction clusters

The normalized histograms of 24-h TC intensity change episodes for the three TC–trough clusters are shown in Fig. 6. TCs in the cutoff cluster are associated

with a broad peak in the distribution of intensity change episodes, with the right side of the peak shifted toward larger intensification rates. In fact, TCs in the cutoff cluster are characterized by statistically significant greater rates of intensification than TCs in the NW and NE trough clusters. TCs in the NW trough cluster are associated with a shift in the intensity change distribution toward lesser rates of TC intensification, which is especially evident in the upper tail of the distribution, denoted by a relative lack of RI episodes.

The number of unique TCs, RI episodes, and non-RI episodes in each TC–trough configuration cluster is provided in Table 2. Interestingly, TCs in the cutoff and NE trough clusters are more than twice as likely to undergo RI as TCs in the NW trough cluster, as 7.1% and 6.7% of TC intensity change episodes in the cutoff and NE trough clusters meet the criterion for RI, compared to only 3.1% of TC intensity change episodes in NW trough cluster. A caveat to this result arises from treating each 24-h TC intensity change episode as a unique entity. In reality, the potential for autocorrelation exists by using overlapping 24-h TC intensity change episodes
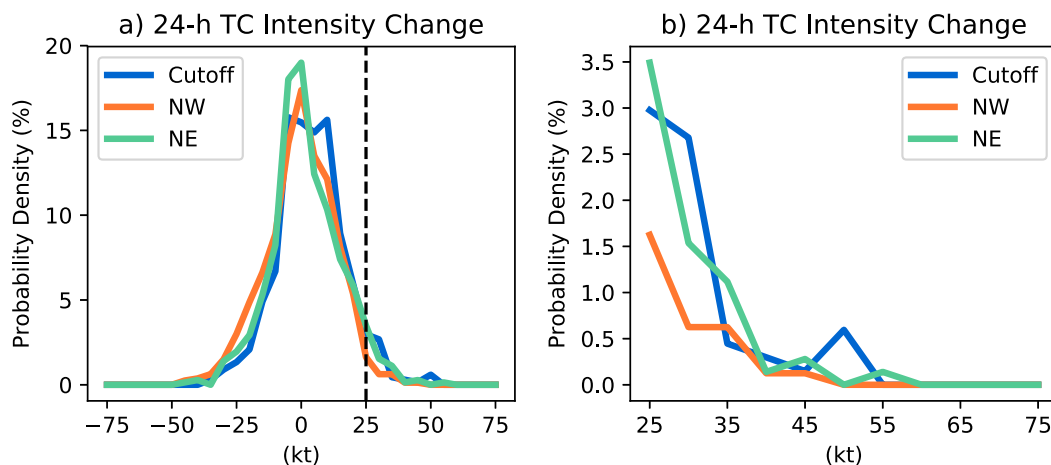
FIG. 6. (a) Normalized histogram (%) of 24-h TC intensity change (kt) for high-PV TCs in the North Atlantic basin from 1989 to 2016. The intensity change distributions are grouped by the TC–trough configuration cluster, where TCs in the cutoff cluster, NW trough cluster, and NE trough cluster are represented by blue, orange, and green lines, respectively. The bin interval is 5 kt. The black, dashed, vertical line denotes the threshold for RI (25 kt). (b) As in (a), but focused on the frequency of cases with a 24-h TC intensity change ≥ 25 kt. Note the difference in scaling along the ordinate.

within the same, or in some cases, different clusters. This caveat should also be considered any time statistical significance is computed in this study, as a smaller effective sample reduces the likelihood that a given difference will be statistically significant.

The locations of the TCs at the onset of both RI and non-RI episodes that comprise each TC–trough interaction cluster are shown in Fig. 7. TCs in the cutoff cluster generally occur more poleward and eastward than TCs in the other two clusters (Fig. 7a). The distributions of both latitude and longitude for TCs in the cutoff cluster are statistically significantly different than those for TCs in the NW and NE trough clusters. TCs within the NW and NE trough clusters exhibit more latitudinal spread, with more cases in the Gulf of Mexico and Caribbean Sea than the cutoff cluster (Figs. 7b,c). TCs in the NW trough cluster occur significantly more equatorward than TCs within the cutoff and NE trough clusters. RI episodes in the NW and NE trough clusters occur significantly more westward than non-RI episodes in the corresponding cluster, although no significant differences in the locations of RI and non-RI episodes were found in the cutoff cluster.

5. The relationship between upper-tropospheric trough structure and RI

The upper-tropospheric trough morphology and evolution for each TC–trough configuration cluster is presented via lag composites of PV and wind at 200 hPa. Although each cluster was initially created based on PV anomalies on the 350-K isentropic surface, the climatological average height of the 350-K isentropic surface in the subtropical North Atlantic between July–December, when the majority of the analyzed TC–trough interactions occurred, is close to the 200-hPa isobaric surface (not shown). By performing composite analyses on the 200-hPa isobaric surface, direct comparisons with previous studies, such as Hanley et al. (2001), can be made.

a. Characteristics of the cutoff cluster

Figure 8 depicts the storm-centered, composite-mean, 200-hPa PV and winds for RI and non-RI episodes in the cutoff cluster over a 24-h period, beginning 12 h prior to the onset of the intensity change episode. TCs in the cutoff cluster are characterized by upper-tropospheric troughs located directly over and immediately to the southwest of the TC (Fig. 8). The composites of TC–trough interactions in the cutoff cluster resemble the composites of "superposition" TC–trough interactions analyzed by Hanley et al. (2001). In each composite, the upper-tropospheric trough is associated with a local

TABLE 2. Number of unique TCs (Unique TCs), as well as total number of TC intensity change episodes for all high-PV TCs (All), number of rapid intensification episodes (RI), and number of nonrapid intensification episodes (non-RI) sorted by TC–trough configuration cluster.

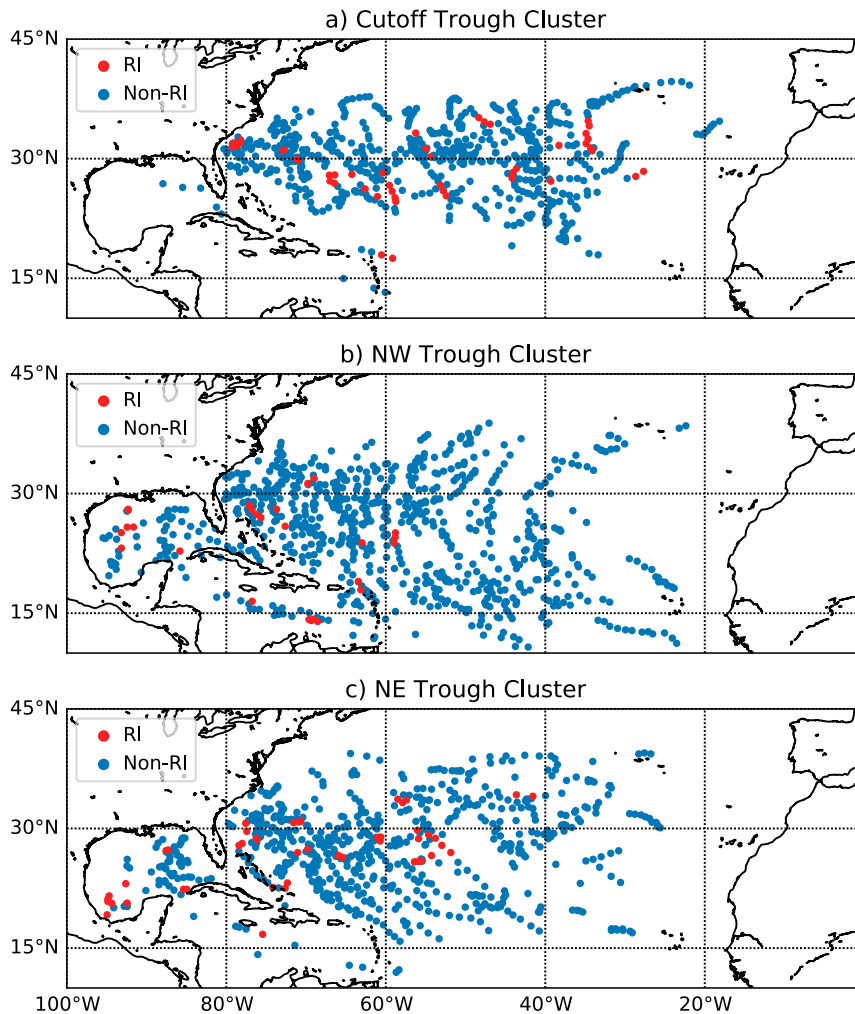| Cluster	Unique TCs	All	RI	Non-RI
Cutoff	88	672	48	624
NW trough	171	800	25	775
NE trough	137	716	48	668

FIG. 7. Geographic locations of the 850-hPa relative vorticity centroids for RI episodes (red) and non-RI episodes (blue) for high-PV TCs within the (a) cutoff cluster, (b) NW trough cluster, and (c) NE trough cluster.

maximum in PV that is partially detached from the poleward reservoir of high PV, resembling a cyclonic wave-breaking event (Thorncroft et al. 1993), and a secondary maximum in wind speed observed on the south side of the TC (Figs. 8a–f). RI episodes within the cutoff cluster are consistently associated with regions of statistically significant weaker PV within the core of the upper-tropospheric trough than non-RI episodes (Figs. 8g–i). The zonal scale of the composite upper-tropospheric troughs for RI episodes is approximately 1000 km (Figs. 8a–c), which is nearly half the scale of the troughs in the non-RI composite (Figs. 8d–f). These findings are consistent with previous work that suggested smaller-scale upper-tropospheric PV anomalies are more favorable for TC intensification during TC–trough superposition (Molinari et al. 1995, 1998).

The maximum PV values associated with the upper-tropospheric troughs in the RI composites are located approximately 250–500-km farther upstream of the TC center than those in the non-RI composites (Figs. 8a–f). Additionally, RI episodes are consistently associated with weaker 200-hPa wind speeds on the south side of the TC (Figs. 8a–c) than non-RI episodes (Figs. 8d–f). RI episodes display an amplification of the downstream ridge that occurs in tandem with an increase in 200-hPa PV associated with the upstream trough (Figs. 8a–c). Conversely, in non-RI episodes, the areal extent of regions with >2.0 PVU decreases with time (Figs. 8d–f).

Differences in the vertical structure of the upper-tropospheric troughs associated with RI and non-RI episodes in the cutoff cluster are examined in southwest–northeast, vertical cross sections, centered on the TC location (Fig. 9). The axes along which the vertical cross
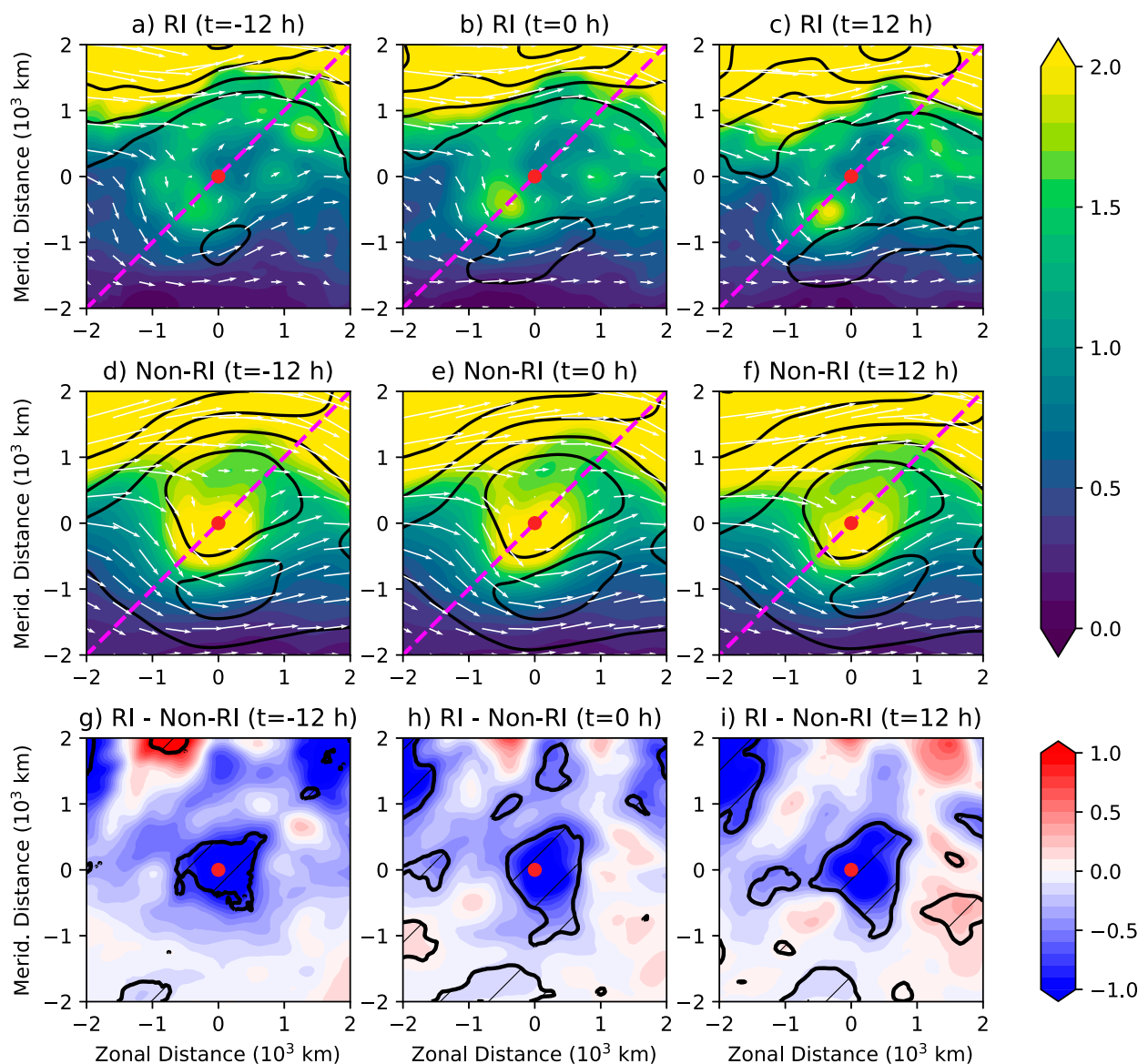
FIG. 8. Composite-mean, storm-centered, 200-hPa PV (PVU; shaded) and winds (white arrows) for RI episodes in the cutoff cluster (a) 12 h prior to the onset of the intensity change episode, (b) at the onset of the intensity change episode, and (c) 12 h after the onset of the intensity change episode. The zonal and meridional distance (10^3 km) from the TC center is displayed along the abscissa and ordinate of each plot, respectively. Wind speed (black contours) are shown every $5\,\mathrm{m\,s^{-1}}$ for values $\geq 10\,\mathrm{m\,s^{-1}}$. The dashed, magenta line in each panel denotes the axis along which vertical cross sections are taken in Fig. 9. (d)–(f) As in (a)–(c), but for non-RI episodes. (g)–(i) Difference in PV (PVU; shaded) between RI–non-RI composites at $t = -12$, $t = 0$, and $t = 12$ h, respectively. Black contours and hatching indicate differences that are statistically significant at the 95% confidence level.

sections were taken are displayed by the dashed, magenta lines in Fig. 8. In the composites of both RI and non-RI episodes, the reanalysis is able to crudely resolve the PV tower associated with the composite TC, depicted by a local maximum in PV within 250 km of the TC location, spanning approximately 1000–300 hPa (Figs. 9a–f). In both RI and non-RI episodes, a local PV maximum is observed near, and immediately upstream of, the TC location at 200 hPa, consistent with Fig. 8.

The composites of RI episodes (Figs. 9a–c) are associated with upstream upper-tropospheric troughs of smaller spatial scales, as well as less PV immediately above the TC center than non-RI episodes (Figs. 9d–f). The differences in vertical structure of PV between RI and non-RI episodes in the cutoff cluster are more apparent in the difference plots shown in Figs. 9g–i. At each lag time, RI episodes are associated with less upper-tropospheric PV than non-RI episodes within approximately 750 km of the
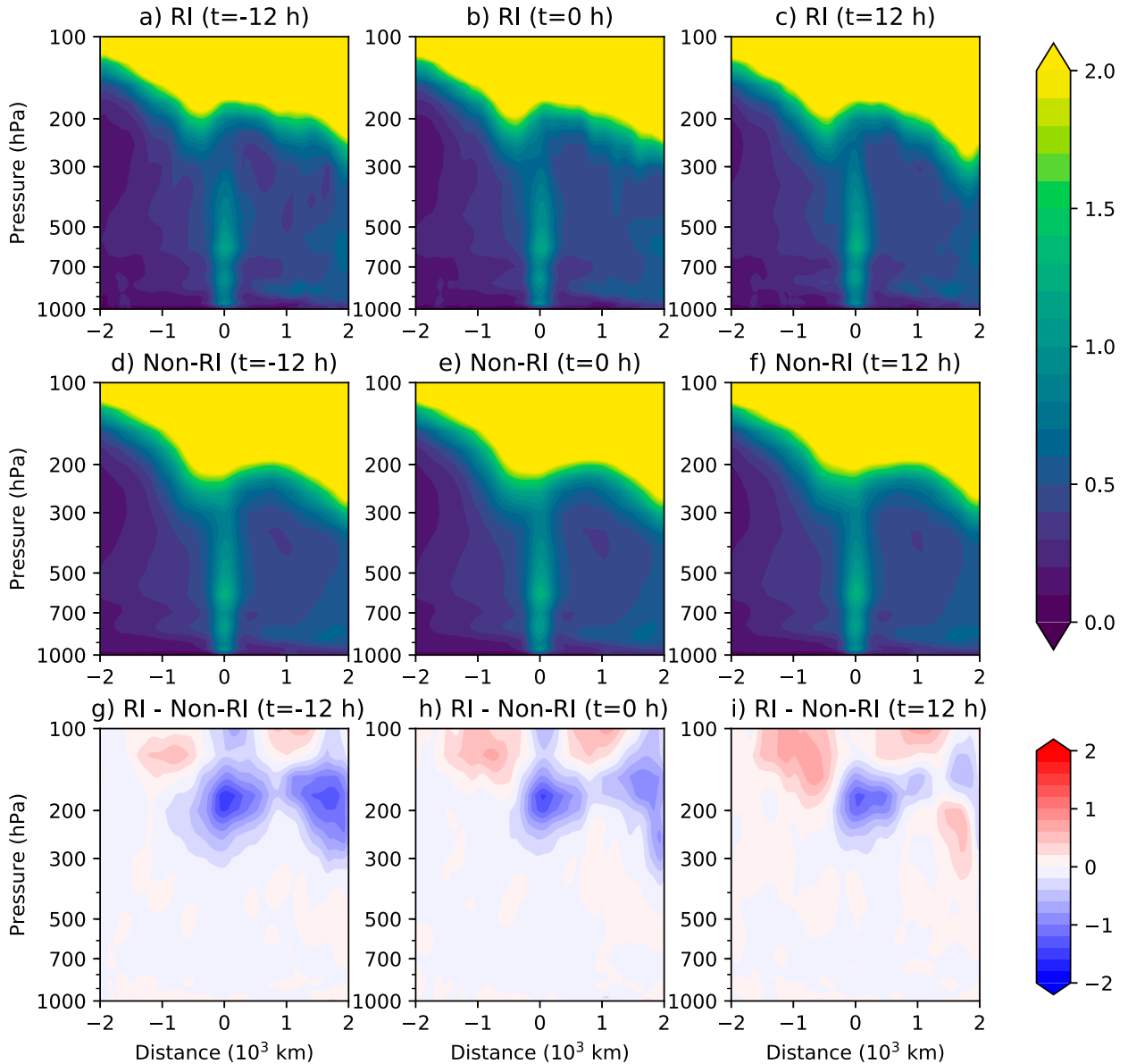
FIG. 9. Composite-mean, storm-centered, vertical cross sections of PV (PVU; shaded) for RI episodes in the cutoff cluster (a) 12 h prior to the onset of the intensity change episode, (b) at the onset of the intensity change episode, and (c) 12 h after the onset of the intensity change episode. Cross sections are taken from 2000 km southwest of the TC (negative distance), through the TC location, to 2000 km northeast of the TC (positive distance). (d)–(f) As in (a)–(c), but for non-RI episodes. (g)–(i) As in (a)–(c), but for the difference between RI and non-RI episodes.

TC location between 300 and 150 hPa. The difference between composites becomes slightly less pronounced with time, which is consistent with the increase in PV upstream of RI episodes, as well as the decrease in spatial extent of the composite upper-tropospheric trough in non-RI episodes, seen in Fig. 8.

b. Characteristics of the NW trough cluster

The composites of 200-hPa PV and winds for TCs in the NW trough cluster (Fig. 10) are associated with a

much different TC–trough configuration than the cutoff cluster. The upper-tropospheric troughs that comprise the NW trough cluster are located farther from the TC than the composite troughs in the cutoff cluster and display a positive tilt, devoid of prominent wave breaking within 1000 km of the TC center. The TC–trough configurations in the NW trough cluster resemble the "distant" TC–trough interactions analyzed by Hanley et al. (2001). In both RI and non-RI episodes, the upper-tropospheric trough approaches the location of the
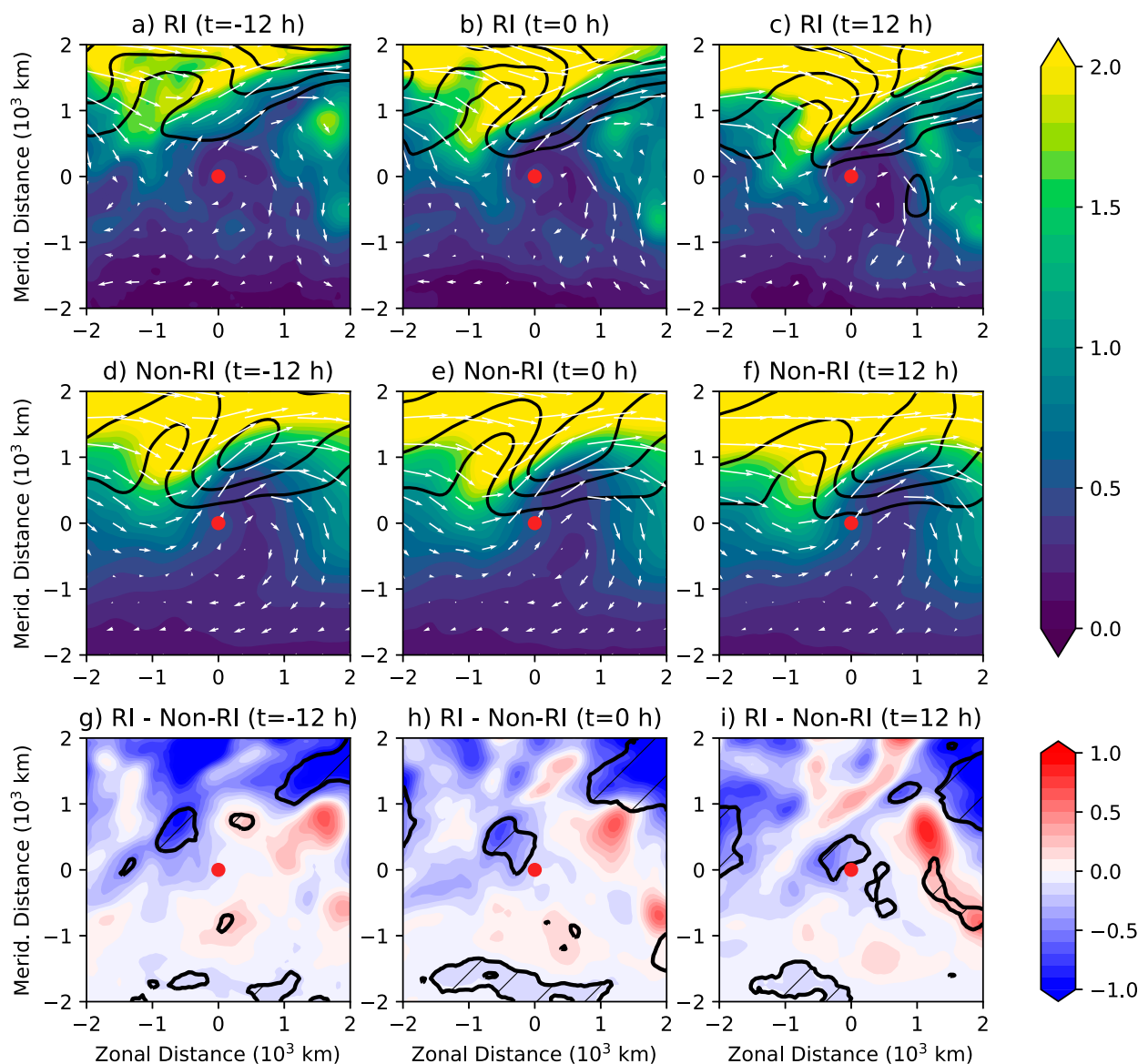
FIG. 10. As in Fig. 8, but for TCs in the NW trough cluster.

TC; however, the upper-tropospheric trough in the RI composite remains farther upstream. Consistent with the greater upstream trough displacement, the RI composites are associated with regions of significantly weaker 200-hPa PV approximately 0–1000 km to the northwest of the TC at all lead times (Figs. 10g–i). This region of statistical significance approaches, and becomes nearly collocated with, the TC during the TC intensity change episode.

In each of the NW trough cluster composites, anticyclonic flow is observed at 200 hPa near, and downstream of, the TC (Figs. 10a–f). The upstream troughs in the RI composites are also associated with a shorter zonal wavelength and a sharper PV gradient between the TC

and the base of the trough, especially at $t = 0$ and $t = 12$ h (Figs. 10b,c). In both the RI and non-RI composites, a 200-hPa jet is observed to the northeast of the TC center (Figs. 10a–f). Although the jet strengthens with time in the RI composites, stronger 200-hPa wind speeds are consistently observed within 500 km of the TC location in the non-RI composites (Figs. 10d–f). The magnitude of PV associated with the troughs in the RI composites increases with time (Figs. 10a–c), similar to the pattern observed with TCs in the cutoff cluster (Figs. 8a–c).

c. Characteristics of the NE trough cluster

The upper-tropospheric trough morphologies associated with TCs in the NE trough cluster (Fig. 11) have
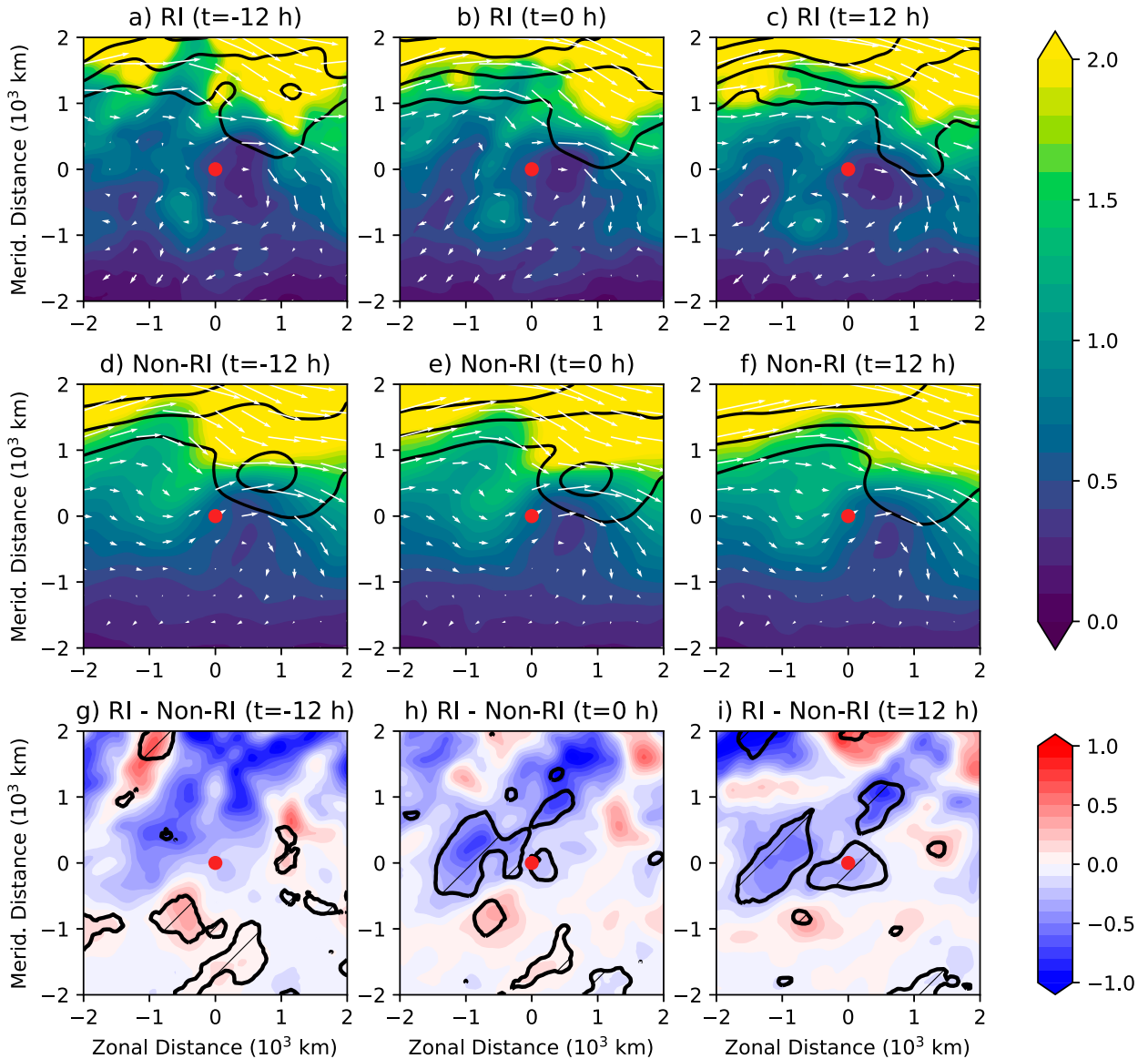
FIG. 11. As in Fig. 8, but for TCs in the NE trough cluster.

the highest PV located northeast of the TC. The upper-tropospheric troughs in both the RI and non-RI composites display a positive tilt, but large differences are observed at the base of the trough. The composites of RI episodes in the NE trough cluster display a trough fracture near the base of the trough, with a secondary, weak maximum in PV existing to the southwest of the TC at all analyzed times (Figs. 11a–c). The secondary maximum in PV drifts slowly southward, away from the TC with time. RI episodes are associated with regions of significantly weaker 200-hPa PV near, and to the northwest of, the TC at $t = 0$ and $t = 12$ h, consistent with the evolution of a trough fracture (Figs. 11h,i).

Adjacent to the location of the trough fracture, two regions of weak, anticyclonic flow are observed: one to the west and one the east of the fracture. The resulting flow pattern resembles a col, with minimal flow observed over the TC (Figs. 11a–c). Non-RI episodes in the NE trough cluster are associated with stronger, westerly flow over the TC, as the upstream trough does not fracture and remains a positively tilted PV streamer (Figs. 11d–f). The non-RI composites also display two regions of anticyclonic flow, but the upstream region is located farther poleward, and the downstream region located farther equatorward, than the locations of anticyclonic flow in the RI composites.

6. Environmental characteristics of each trough cluster

Previous work has shown upper-tropospheric troughs tend to be associated with increased environmental vertical wind shear (Hanley et al. 2001) and relatively dry midtropospheric air (Zhang et al. 2016), both of which can act to ventilate the TC warm core with relatively low-entropy environmental air. One of the goals of the current study is to determine how the environmental favorability for TC intensification is related to the upper-tropospheric trough morphology. To assess the environmental favorability for TC intensification, a modified version of the ventilation index of Tang and Emanuel (2012) was employed. Lower values of the ventilation index are more favorable for TC intensification, including RI (Tang and Emanuel 2012; Lin et al. 2017). Here, we define the ventilation index as

$$\Lambda = \frac{u_{\text{shear}} \chi_m}{u_{\text{PI}}}, \qquad (2)$$

where u_{shear} is the 1000–250-hPa environmental vertical wind shear magnitude, χ is the entropy deficit, the subscript m indicates the azimuthal mean, and u_{PI} is the MPI. The 1000–250-hPa layer was chosen for the vertical wind shear calculation, as this layer was found to have a stronger correlation to future 24-h TC intensity change than the 850–200-hPa layer used by Tang and Emanuel (2012). The entropy deficit is defined as

$$\chi = \frac{s_m^* - s_m}{s_{\text{SST}}^* - s_b}, \qquad (3)$$

where s_m^* is the average saturation entropy at 600 hPa in the inner core of the TC (≤ 100 km), s_m is the entropy at 600 hPa averaged within an 100–300-km TC-centered annulus, s_{SST}^* is the saturation entropy at the sea surface temperature, and s_b is the entropy of the boundary layer. Essentially, for a given TC, χ represents the difference in moist entropy between the TC inner core and the environment, divided by the air–sea disequilibrium at the MPI. Following Tang and Emanuel (2012), the calculation of Eq. (3) utilizes the pseudoadiabatic entropy from Bryan (2008). Although the relatively coarse spatial resolution of the reanalysis may yield biased estimates of χ and Λ, the purpose of this analysis is to compare the distributions of χ and Λ for both RI and non-RI episodes in each trough cluster. Any potential resolution-driven biases associated with the reanalysis should be consistent for all intensity change episodes and trough clusters.

Figure 12a shows the distributions of Λ for RI and non-RI episodes in each TC–trough cluster. RI episodes are consistently associated with statistically significant

lower Λ values than non-RI episodes in each cluster. The interquartile ranges of Λ seen in RI and non-RI episodes in a given TC–trough cluster only display a slight overlap. These results indicate less ventilation of the TC with low-entropy environmental air during trough interaction events is favorable for RI.

To assess whether the differences in Λ between RI and non-RI episodes are driven by one particular component of Λ, Figs. 12b–d show the distributions of the deep-layer vertical wind shear magnitude (u_{shear}), the environmental entropy deficit (χ_m), and the environmental MPI (u_{PI}) for both RI and non-RI episodes. Figure 12b shows RI episodes are associated with statistically significant weaker vertical wind shear magnitudes than non-RI episodes in each cluster. Nonetheless, in each TC–trough cluster, an overlap in the distribution of shear for RI and non-RI episodes exists, suggesting that although RI is favored in environments of lower vertical wind shear, RI is still possible when the 1000–250-hPa shear exceeds 5–6 m s^{-1}, especially for TCs in the NW trough cluster (Fig. 12b). The observance of RI in moderate levels of vertical wind shear is consistent with the modeling simulations of Zhang and Tao (2013), Judt and Chen (2016), and Rios-Berrios et al. (2018).

Similar to the distributions of vertical wind shear, RI episodes in each cluster are also consistently associated with significantly lower χ_m, indicative of a more favorable thermodynamic environment (Fig. 12c). RI episodes in the cutoff cluster generally have the largest χ_m of the three RI groups, which is consistent with their more poleward locations (Fig. 7).

Unlike the other parameters displayed in Fig. 12, the distributions of MPI display some cluster dependency, as seen by the lower MPI for TCs in the cutoff cluster compared to TCs in the NW and NE trough clusters (Fig. 12d). In fact, the median MPI for RI episodes in the cutoff cluster is less than 80 m s^{-1}, which is less than the median value of non-RI episodes in the NW and NE trough clusters. Again, the lower environmental MPI of TCs in the cutoff cluster is likely linked to their more poleward locations (Fig. 7). The distributions of MPI for TCs in the NW and NE trough clusters are relatively similar. Regardless, in each cluster, RI episodes are associated with significantly larger environmental MPI than non-RI episodes in the corresponding cluster. This result indicates that *anomalous* environmental MPI, relative to a given upper-tropospheric trough morphology, may be more important for RI than the observed MPI during a TC–trough interaction event.

To quantify the relationship between TC environmental conditions and TC intensity change, Table 3 shows the correlation coefficients for various environmental parameters and future 24-h intensity change. Generally, the
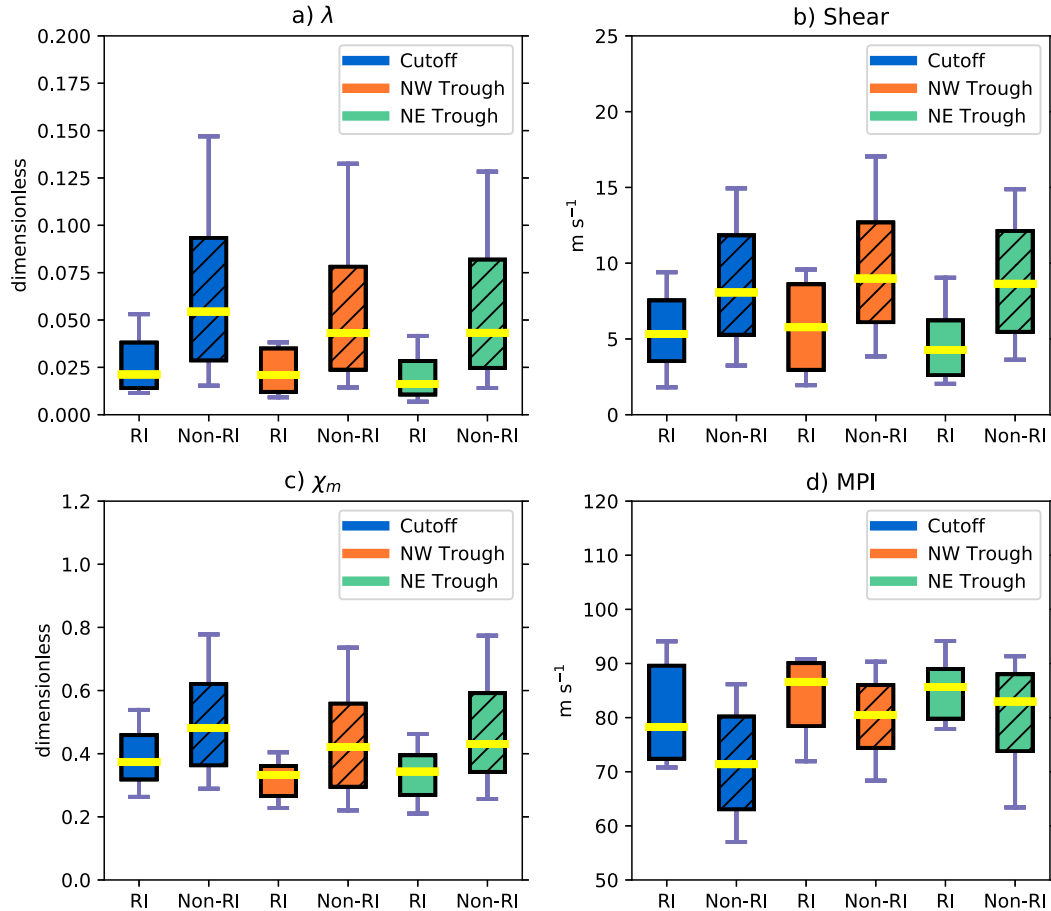
FIG. 12. Box-and-whisker plots of (a) ventilation index (Λ; dimensionless) for RI and non-RI episodes within the cutoff cluster (blue), NW trough cluster (orange), and NE trough cluster (green), at the onset of the intensity change episode ($t = 0$ h). The boxes range from the 25th–75th percentiles of the distribution, with a yellow line depicting the median, while the whiskers span the 10th–90th percentiles. Boxes with black hatching indicate the given intensity change group is associated with a statistically significant different distribution from RI episodes within the corresponding cluster at the 95% confidence level. Recall that the number of effective samples (i.e., the number of unique TCs) differs from the number of total TC intensity change episodes, as seen in Table 2. Here, statistical significance was determined using all TC intensity change episodes within a given intensity change group, rather than only using unique samples. (b)–(d) As in (a), but for 1000–250-hPa vertical wind shear magnitude (m s^{-1}), entropy deficit (χ_m; dimensionless), and MPI (m s^{-1}), respectively.

correlation coefficients associated with Λ display the largest absolute values. Because Λ is characterized by a logarithmic distribution, a more suitable correlation metric may be a rank correlation, rather than the Pearson correlation coefficient shown in Table 3. Indeed, when rank correlations between Λ and intensity change are computed, the correlation coefficients are generally 0.03–0.06 greater than those in Table 3 (not shown). Regardless, these findings demonstrate the ventilation of the TC inner core, as estimated by Λ, has a strong influence on TC intensification during TC–trough interactions, especially for TCs in the cutoff and NE trough clusters. Of the three components of Λ, the correlations between χ_m and intensity change were consistently the

most robust. Among each variable displayed in Table 3, TCs in the NW trough cluster generally display the smallest correlation coefficients, suggesting that in such trough configurations, more of the intensity change variability is controlled by factors other than ventilation.

7. Convective characteristics of TC–trough interactions

a. A comparison of the convective characteristics of TCs in high- and low-PV environments

Performing a robust composite analysis of TC convective characteristics when examining a range of TC intensities is challenging due to the strong relationship

TABLE 3. Pearson correlation coefficients of 24-h intensity change and ventilation index parameters for all high-PV TCs, and TCs within the cutoff, NW trough, and NE trough clusters, respectively. Correlations were calculated using parameters obtained at the onset of the intensity change episode ($t = 0$ h).

TC group	Λ	u_{shear}	χ_m	u_{PI}
All	−0.27	−0.23	−0.25	0.19
Cutoff	−0.37	−0.22	−0.35	0.34
NW trough	−0.17	−0.17	−0.19	0.14
NE trough	−0.33	−0.29	−0.28	0.23

between TC convective structure and TC intensity (e.g., Dvorak 1975; Cecil and Zipser 1999; Velden et al. 2006). A novel approach to bypass this issue was introduced by Fischer et al. (2018), who developed a convective normalization technique that identifies the anomalous convective characteristics of a TC relative to the convective structure typically associated with TCs of similar intensities. Considering the TC–trough interactions analyzed within the present study span a wide range of TC intensities, the convective normalization technique of Fischer et al. (2018) provides a method to directly relate the convective structures of TC–trough interactions to the rate of intensity change.

As in Fischer et al. (2018), normalized IR and microwave brightness temperatures were computed following:

$$T_b^* = \frac{T_b - \overline{T_b}}{\sigma}, \qquad (4)$$

where T_b^* is the normalized brightness temperature, T_b is the observed brightness temperature, $\overline{T_b}$ is the mean of the climatological brightness temperature, and σ is the standard deviation of the climatological brightness temperature. The normalization is computed in a shear-relative framework, using the deep-layer (1000–250-hPa) shear vector. The climatological brightness temperatures are obtained from TCs of similar intensities to the TC of interest. To summarize, anomalously low IR brightness temperatures are indicative of anomalously low cloud top temperatures, consistent with anomalously vigorous convection, while the converse is also true. Similarly, anomalously low 85-GHz brightness temperatures indicate anomalously large frozen hydrometeor content, while anomalously high 37-GHz brightness temperatures generally indicate anomalously large liquid hydrometeor content (Fischer et al. 2018).

Before an analysis of the normalized convective characteristics of each TC–trough configuration cluster is performed, it is important to understand how the normalized convective characteristics of TCs with nearby upper-tropospheric troughs (high-PV TCs) differ from

TCs in environments devoid of upper-tropospheric troughs (low-PV TCs). Figure 13 shows normalized IR, 37, and 85-GHz brightness temperatures for both high- and low-PV TCs. Here, the normalization was performed using climatological brightness temperatures derived from all TCs, regardless of the type of environment in which they were located, as in Fischer et al. (2018). From Fig. 13, TCs in high-PV environments tend to have positive, normalized IR and 85-GHz brightness temperatures, as well as negative, normalized 37-GHz brightness temperatures (Figs. 13a–c). These results indicate TCs interacting with a nearby upper-tropospheric trough are typically associated with anomalously weak convection. Conversely, TCs in low-PV environments are associated with anomalously low IR brightness temperatures and anomalously large liquid and ice hydrometeor content (Figs. 13d–f), consistent with anomalously vigorous convection. The difference plots shown in Figs. 13g–i indicate large regions of statistical significance within the innermost 400 km of the TC center. In each normalized frequency, the differences between low- and high-PV TCs are most pronounced in the upshear-right quadrants. Because low-PV TCs are associated with significantly larger TC intensification rates than TCs in high-PV environments (Fig. 3), these results are consistent with the findings of Zagrodnik and Jiang (2014), Alvey et al. (2015), Tao and Jiang (2015), and Fischer et al. (2018), who determined the presence of anomalously vigorous, upshear convection is important for greater TC intensification rates. The more vigorous anomalous convective activity observed in low-PV TCs is also consistent with more favorable environmental conditions, characterized by lower Λ (not shown).

b. Convective characteristics of RI episodes in unique TC–trough configurations

Figure 14 presents the normalized IR brightness temperatures for both RI and non-RI episodes in each TC–trough configuration cluster. For reference, the number of intensity change episodes with available satellite data is provided in Table 4. In each cluster, RI episodes feature a region of anomalously low IR brightness temperatures throughout much of the innermost 200 km (Figs. 14a–c). RI episodes in the NW trough cluster are associated with the lowest, normalized, IR brightness temperatures (Fig. 14b), whereas RI episodes in the cutoff cluster are associated with the least-negative, normalized IR brightness temperatures (Fig. 14a). The anomalous TC convective structures in each trough cluster display similarities with their respective thermodynamic environmental conditions, as RI episodes in the cutoff cluster tend to have smaller MPIs compared to the MPI distributions of the other RI groups, whereas RI
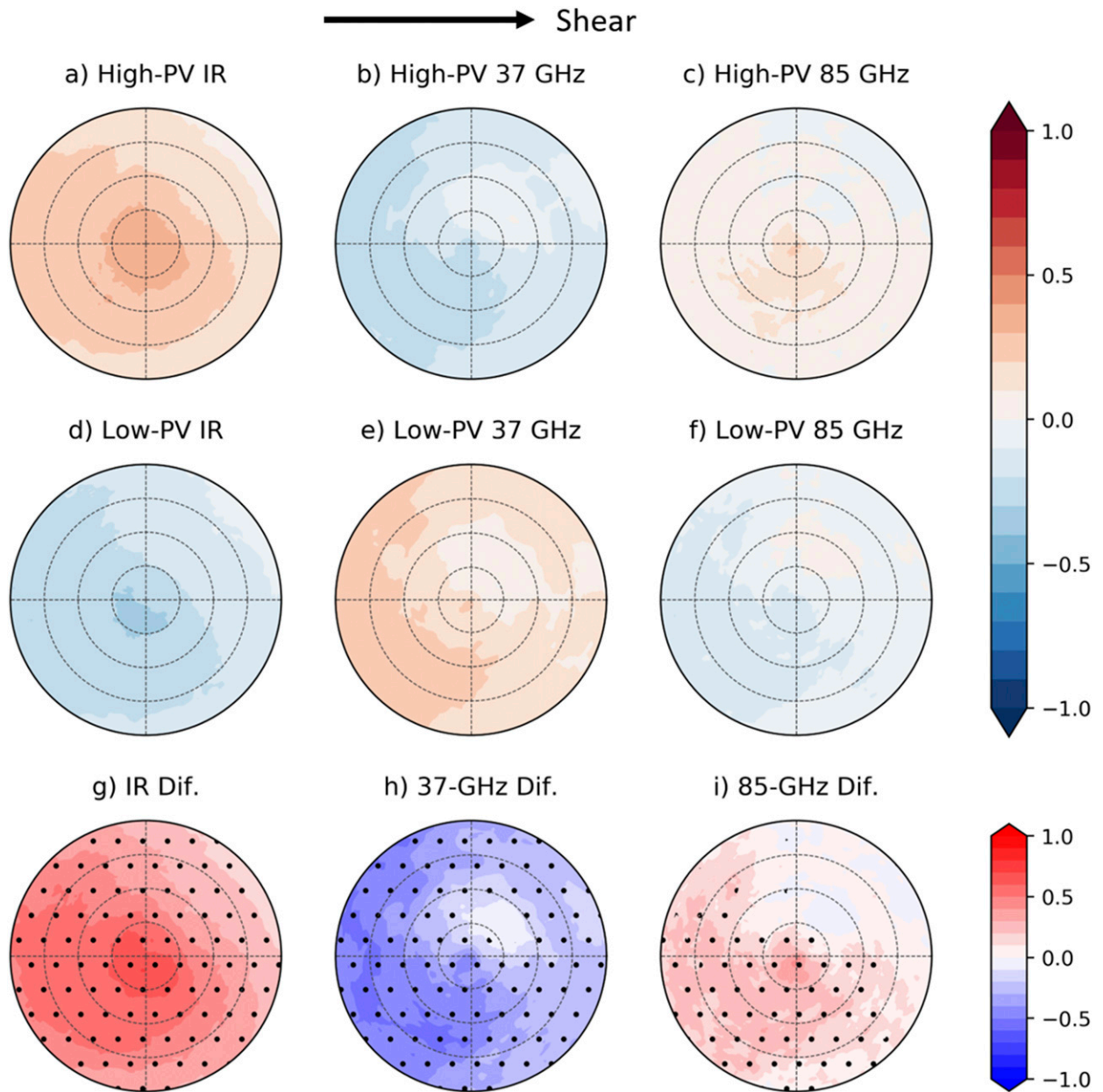
FIG. 13. Composite-mean, storm-centered, shear-relative, normalized (a) IR brightness temperatures, (b) 37-GHz brightness temperatures, and (c) 85-GHz brightness temperatures for all high-PV TCs. Composites are shown at the onset of the intensity change episode ($t = 0$ h). Each composite is rotated by the deep-layer (1000–250 hPa) environmental vertical wind shear direction, with the shear vector pointing to the right side of each panel, as indicated by the black arrow. Radial rings are spaced in 100-km increments. (d)–(f) As in (a)–(c), but for all TCs in low-PV environments. (g)–(i) As in (a)–(c), but for the difference between high-PV TCs and low-PV TCs. The stippling pattern denotes regions where the differences are statistically significant at the 95% confidence level.

episodes in the NW trough cluster tend to have larger MPIs (Fig. 12d). Previous work has shown warmer sea surface temperatures, likely reflected by higher MPIs, are associated with colder tropopause temperatures (e.g., Reid and Gage 1981), manifested here through the lower normalized IR brightness temperatures seen in the NW trough cluster.

The composites of normalized IR brightness temperatures for non-RI episodes in each TC–trough configuration cluster are characterized by anomalously high IR brightness temperatures throughout nearly the entire innermost 200 km (Figs. 14d–f). Out of the non-RI composites, TCs in the cutoff cluster are associated with the largest normalized IR brightness temperatures (Fig. 14d), and
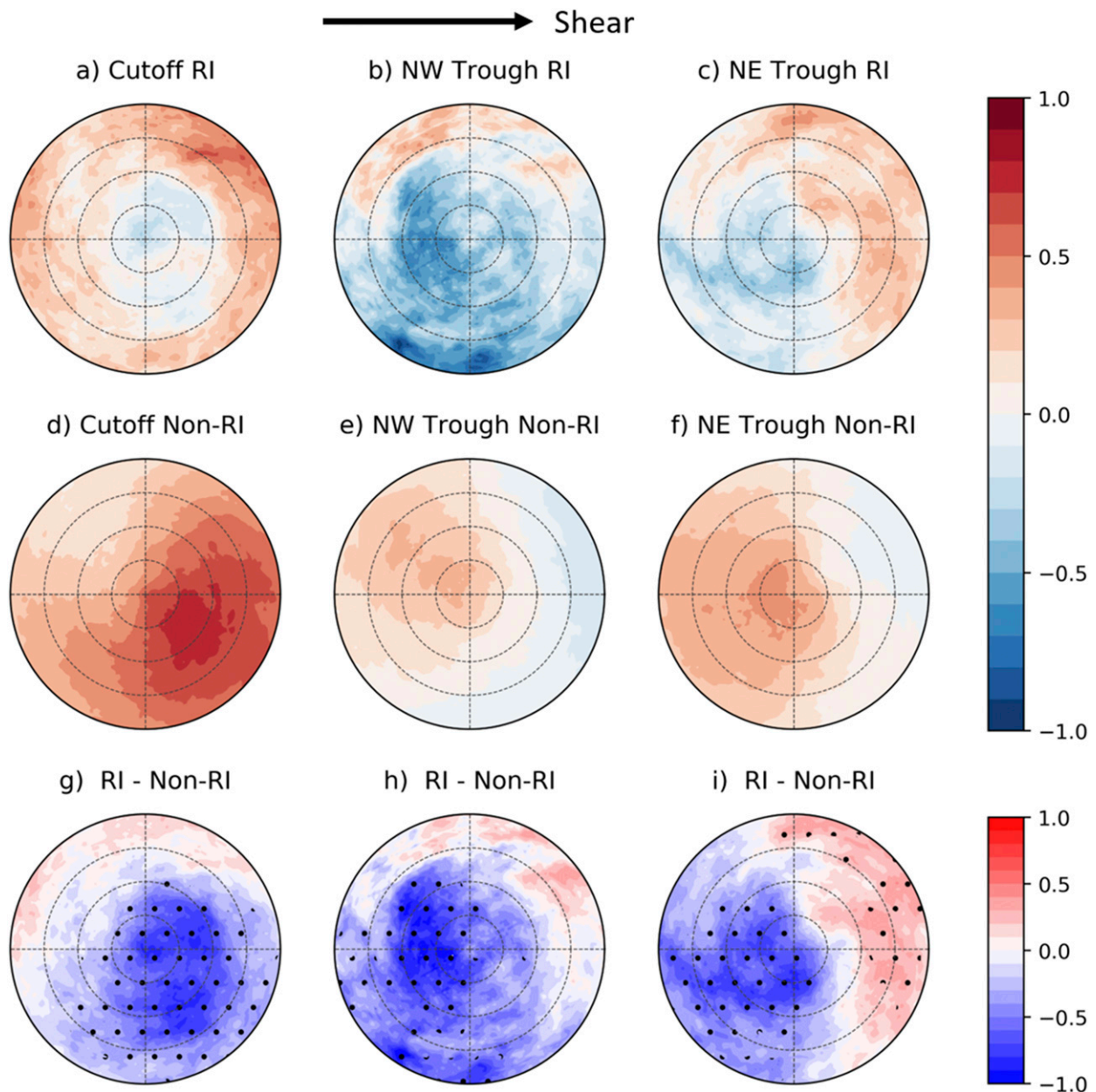
FIG. 14. Composite-mean, storm-centered, shear-relative, normalized IR brightness temperatures for RI episodes in the (a) cutoff cluster, (b) NW trough cluster, and (c) NE trough cluster. Composites are shown at the onset of the intensity change episode ($t = 0$ h). Each composite is rotated by the deep-layer (1000–250 hPa) environmental vertical wind shear direction, with the shear vector pointing to the right side of each panel, as indicated by the black arrow. Radial rings are spaced in 100-km increments. (d)–(f) As in (a)–(c), but for non-RI episodes. (g)–(i) As in (a)–(c), but for the difference between RI episodes and non-RI episodes. The stippling pattern denotes regions where the differences are statistically significant at the 95% confidence level.

non-RI episodes in the NW trough cluster are associated with the smallest maximum in normalized IR brightness temperatures (Fig. 14e). With the exception of the cutoff cluster, the azimuthal locations of the most prominent anomalies are again found in the upshear quadrants (Figs. 14e,f), consistent with the locations noted in the RI composites of the corresponding cluster.

Each TC–trough configuration cluster is associated with large regions of statistically significant differences in normalized IR brightness temperatures (Figs. 14g–i). RI episodes in the cutoff cluster display the largest region of significant differences from non-RI episodes, as well as the greatest downshear extent of significant differences (Fig. 14g). RI episodes in the NW and

TABLE 4. Number of RI and non-RI intensity change episodes with available infrared (IR), 37, and 85-GHz passive microwave imagery for each TC–trough configuration cluster.

Cluster and frequency	Rapid intensification (RI)	Nonrapid intensification (Non-RI)
Cutoff IR	48	623
NW trough IR	24	763
NE trough IR	46	664
Cutoff 37 GHz	25	326
NW trough 37 GHz	13	436
NE trough 37 GHz	20	356
Cutoff 85 GHz	25	319
NW trough 85 GHz	14	409
NE trough 85 GHz	21	342

NE trough clusters are associated with significantly lower normalized IR brightness temperatures, primarily in the innermost 300 km of the upshear semicircle (Figs. 14h,i).

These results demonstrate that although TCs interacting with upper-tropospheric troughs tend to be associated with anomalously high IR brightness temperatures as a whole (Fig. 13a), the presence of anomalously vigorous convection, as indicated by anomalously low IR brightness temperatures, near the TC center is important for RI. Surprisingly, TCs in the cutoff cluster are associated with the greatest TC intensification rates, despite being associated with the largest normalized IR brightness temperatures. Similar to the findings of MPI (Fig. 12d), Fig. 14 indicates the *anomalous* IR brightness temperatures relative to a given TC–trough configuration may be a better indicator of TC intensity change, rather than the *raw value* of the normalized IR brightness temperatures. Unfortunately, the limited sample size of each cluster (Table 4) precludes a robust cluster-relative IR brightness temperature normalization.

To analyze the structure of hydrometeors beneath the cirrus canopy, Figs. 15 and 16 reveal the distribution of anomalous liquid and ice hydrometeors for RI and non-RI episodes in each TC–trough configuration cluster, respectively, using horizontally polarized 37-GHz brightness temperatures and polarization-corrected 85-GHz brightness temperatures, as in Fischer et al. (2018). Here, the sample size of each composite is even smaller than the sample size of the aforementioned normalized IR brightness composites (Table 4) and, thus, the following results should be treated with caution. Nonetheless, recall anomalously high 37-GHz brightness temperatures and anomalously low 85-GHz brightness temperatures indicate regions of anomalously larger liquid and frozen

hydrometeor content, respectively. Similar to the composites of normalized IR brightness temperatures, RI episodes in each cluster are associated with anomalously large liquid and frozen hydrometeor content near the TC center (Figs. 15a–c and 16a–c). Conversely, non-RI episodes tend to be associated with anomalously small liquid and frozen hydrometeor content (Figs. 15d–f and 16d–f).

Although RI episodes in both the cutoff and NE trough clusters are associated with regions of statistically significant larger liquid hydrometeor content within 100 km of the TC center (Figs. 15g,i), RI episodes in the NW trough cluster do not display any regions of statistically significant differences (Fig. 15h). Some regions of significantly greater frozen hydrometeor content for RI episodes in the NW trough cluster, however, are observed in composites of normalized 85-GHz brightness temperature (Fig. 16h). Additionally, RI episodes in the cutoff and NE trough clusters are associated with larger anomalous frozen hydrometeor content around the TC center than non-RI episodes in the corresponding cluster (Figs. 16g,i). These results indicate the presence of anomalously vigorous deep convection is important for RI during TC–trough interactions.

The presence of anomalously vigorous deep convection could have implications on the evolution of a nearby upper-tropospheric trough. For example, more vigorous deep convection would be associated with greater upper-tropospheric divergence and, in turn, potentially greater negative-PV advection by the irrotational wind (e.g., Archambault et al. 2013), acting to keep a nearby trough displaced farther from the TC location. For a fixed upper-tropospheric PV anomaly magnitude, an upper-tropospheric PV anomaly located farther from the TC would induce weaker vertical wind shear over the TC. Such an evolution is consistent with the characteristics of RI episodes in the NW trough cluster.

Alternatively, greater negative-PV advection by the irrotational wind could potentially act to induce an upper-tropospheric Rossby wave-breaking event, causing an upper-tropospheric trough to fracture on approach to the TC (e.g., Bosart et al. 2000; Archambault et al. 2013, 2015; Galarneau et al. 2013). Such an evolution is consistent with the upper-tropospheric trough morphology observed in RI episodes in the cutoff and NE trough clusters, where a secondary PV maximum is located to the southwest of the TC (Figs. 8a–c and 11a–c). The cyclonic circulation associated with the PV maximum to southwest of the TC would partially oppose the climatological westerly midlatitude flow, ultimately reducing the vertical wind shear over the TC and providing a more favorable environment for TC
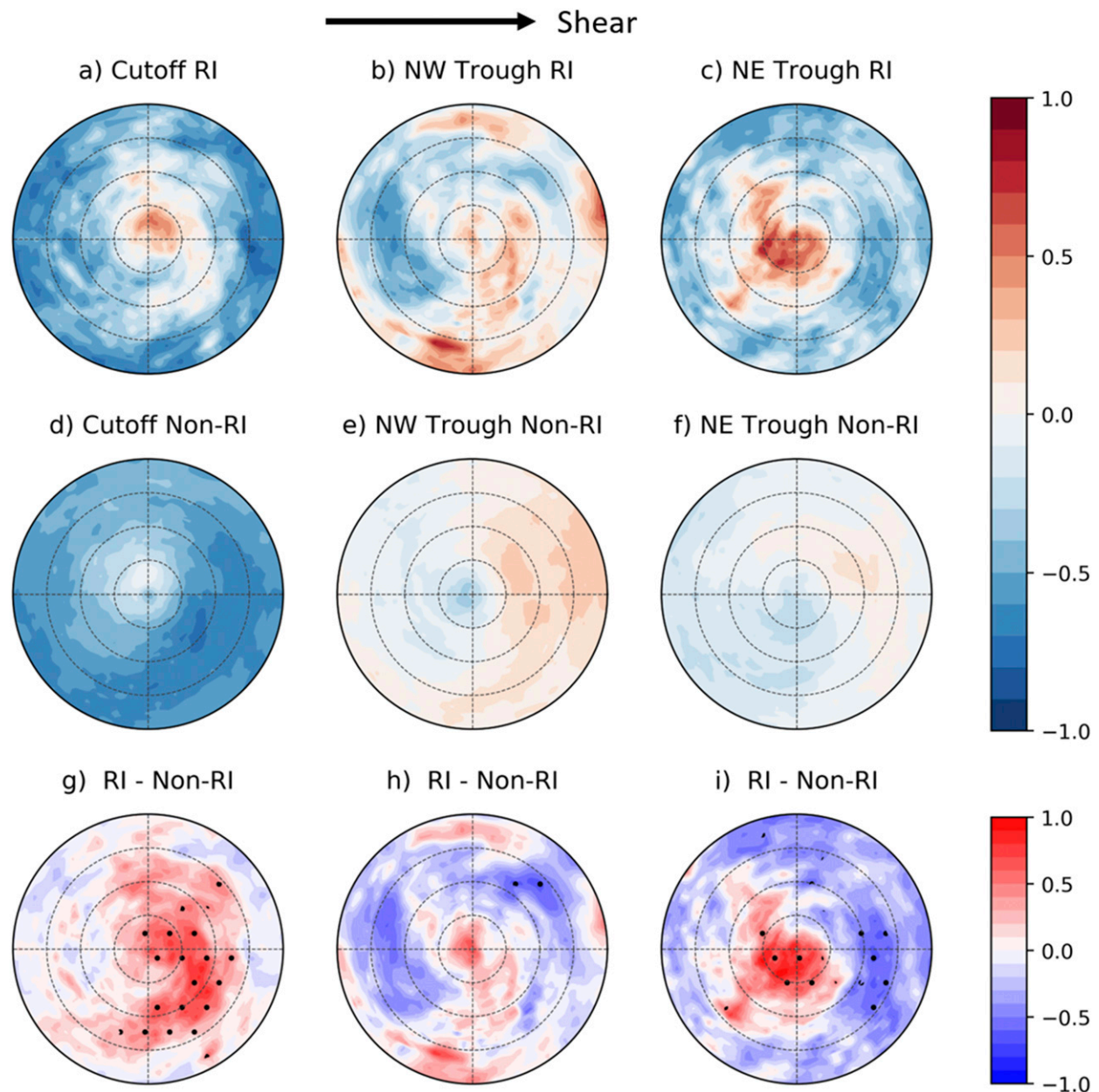
FIG. 15. As in Fig. 14, but for normalized 37-GHz brightness temperatures.

intensification (Rios-Berrios and Torn 2017). In both scenarios, weaker vertical wind shear would favor more symmetric convective development, potentially facilitating a feedback favorable for further TC intensification, including RI.

8. Upper-tropospheric trough forcing for ascent

The strong relationship between RI and anomalously vigorous convection within the TC inner core raises the question of whether the corresponding upper-tropospheric trough configurations induce greater forcing for ascent than the troughs associated with non-RI episodes. Previous work has shown an upper-tropospheric trough acts as a source of angular momentum in the TC outflow layer (Pfeffer and Challa 1981; Molinari and Vollaro 1989). In the framework of a balanced vortex, the eddy flux convergence of angular momentum (EFC) provided by the trough acts to strengthen the TC secondary circulation, potentially invigorating convective activity and causing TC intensification (Molinari and Vollaro 1989, 1990).
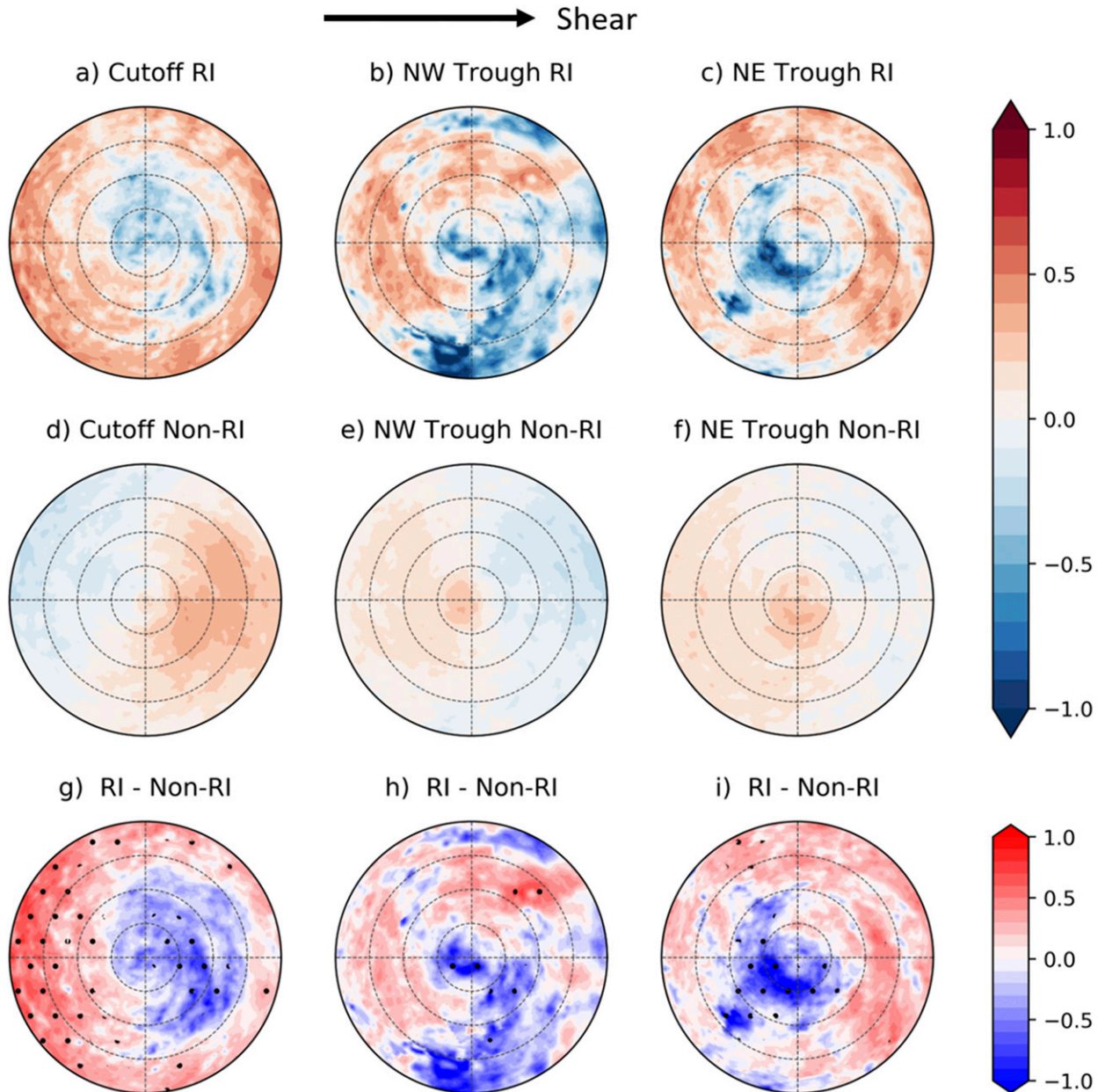
Shear

FIG. 16. As in Fig. 14, but for normalized 85-GHz brightness temperatures.

To examine how EFC is related to RI within each trough cluster, EFC was computed following Molinari and Vollaro (1989):

$$\text{EFC} = -\frac{1}{r^2}\frac{\partial}{\partial r}r^2\overline{u'v'}, \tag{5}$$

where r is the radial distance from the TC, u' is the perturbation of the storm-relative radial wind from the azimuthal mean, v' is the perturbation of the storm-relative tangential wind from the azimuthal mean, and the overbar denotes the azimuthal mean. Figure 17

shows the composite-mean, 200-hPa EFC as a function of time and radius for each trough cluster, as well as the composite-mean differences between RI and non-RI episodes. Of the three TC–trough interaction clusters, TCs in the cutoff cluster are associated with the weakest magnitudes of EFC, which decrease with time (Fig. 17a). In fact, the composite magnitudes of EFC in the cutoff cluster would not satisfy the criteria for a TC–trough interaction episode utilized by previous studies, such as DeMaria et al. (1993), Hanley et al. (2001), and Peirano et al. (2016), which require minimum
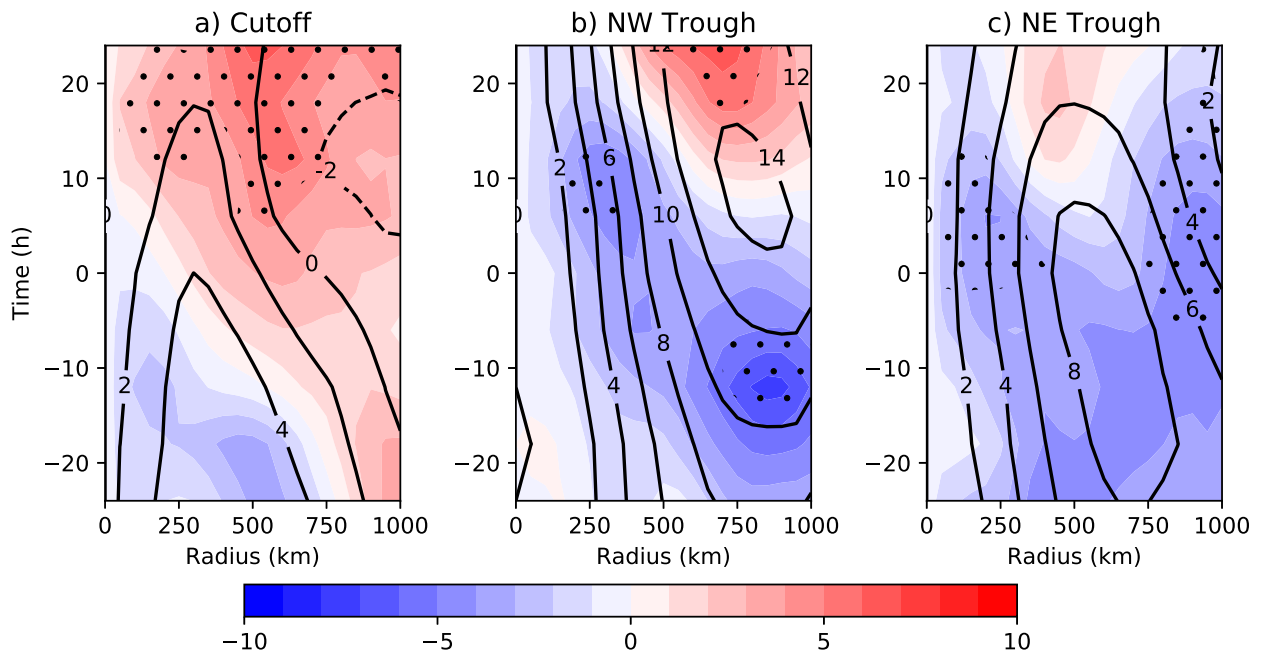
FIG. 17. Composite-mean, 200-hPa eddy flux convergence of angular momentum (EFC; m s^{-1} day^{-1}; black contours) as a function of time (h) relative to the onset of the intensity change episode ($t = 0$ h) for TCs within the (a) cutoff cluster, (b) NW trough cluster, and (c) NE trough cluster. The differences in EFC magnitudes (RI–Non-RI) within the specified cluster are shown in the shading. The stippling pattern denotes regions where the differences are statistically significant at the 95% confidence level.

EFC magnitudes ranging from approximately 7.4–10.0 m s^{-1} day^{-1}, depending on the study. Nonetheless, the composite PV anomalies shown in Fig. 5 demonstrate that upper-tropospheric troughs or cutoff lows can be present near a TC without large values of EFC. The largest values of EFC are found in the composite of the NW trough cluster, with maximum composite-mean values of EFC between 14 and 15 m s^{-1} day^{-1} at $t = 6$–12 h in a radial band approximately 700–900 km from the TC center (Fig. 17b). TCs in the NE trough cluster are associated with maximum composite-mean EFC values greater than TCs in the cutoff cluster, but less than TCs in the NW trough cluster (Fig. 17c). Additionally, the maximum composite-mean EFC values associated with TCs in the NE trough cluster decrease after $t = 0$ h.

The differences between EFC in RI and non-RI episodes are most pronounced for TCs in the cutoff cluster (Fig. 17a). RI episodes have statistically significant greater values of EFC than non-RI episodes, but these differences do not become significant until after $t = 0$ h. RI episodes in the NW trough cluster are consistently associated with weaker magnitudes of EFC than non-RI episodes within the innermost 300 km of the TC (Fig. 17b). Radially outward of 300 km, RI episodes in the NW trough cluster are also associated with significantly weaker EFC than non-RI episodes between approximately $t = -12$ to -6 h within the radial range of

750–1000 km; however, following this time, the sign of the difference begins to reverse, with RI episodes associated with significantly larger EFC values for $t \geq 18$ h. RI episodes in the NE trough cluster are generally associated with weaker EFC than non-RI episodes, with significant differences occurring near $t = 0$ h radially inward of 400 km as well as between 750 and 1000 km.

Correlation coefficients between EFC and TC intensity change at $t = 0$ h are provided in Table 5. The correlations were calculated using averages in two radial bands, between 300–600 and 500–900 km, similar to

TABLE 5. Pearson correlation coefficients of 24-h intensity change and EFC for all high-PV TCs, and TCs within the cutoff, NW trough, and NE trough clusters, respectively. Correlations were calculated using parameters obtained at the onset of the intensity change episode ($t = 0$ h). EFC$_i$ and EFC$_o$ were calculated as the mean 200-hPa eddy flux convergence of angular momentum within 300–600 and 500–900 km of the TC center, respectively. sEFC$_i$ and sEFC$_o$ follow EFC$_i$ and EFC$_o$, respectively, but are the partial correlation coefficients between 200-hPa EFC and the future 24-h TC intensity change after accounting for the magnitude of the 1000–250-hPa vertical wind shear at $t = 0$ h.

TC group	EFC$_i$	EFC$_o$	sEFC$_i$	sEFC$_o$
All	0.03	−0.01	0.07	0.04
Cutoff	0.23	0.21	0.22	0.20
NW trough	−0.09	−0.09	−0.04	−0.03
NE trough	0.00	−0.04	0.08	0.05

Hanley et al. (2001) and Peirano et al. (2016). Although the distribution of EFC associated with all high-PV TCs displays little correlation to intensity change, similar to the findings of DeMaria et al. (1993) and Peirano et al. (2016), EFC does display a more robust correlation with TC intensity change for TCs in the cutoff cluster. In fact, the EFC correlation coefficient for TCs in the cutoff cluster is comparable to that of vertical wind shear (Table 3). These results suggest that the skill associated with using EFC as a predictor of TC intensity change may be dependent on the type of TC–trough interaction.

It is not clear why TC intensity change displays a stronger correlation to EFC for TCs in the cutoff cluster. One possible explanation is that for TCs in environments of relatively weak EFC, such as those TCs in the cutoff cluster, TC intensification itself may lead to an increase in EFC. For example, it is likely that an intensifying TC is associated with greater convective activity (e.g., Zagrodnik and Jiang 2014; Tao and Jiang 2015; Fischer et al. 2018), which would favor stronger, anticyclonic outflow. If the stronger outflow from the intensifying TC is asymmetric, it will yield more positive EFC values, as the anticyclonic outflow is expelled away from the TC [Eq. (5)]. Because the magnitude of EFC is not significantly different for RI and non-RI episodes in the cutoff cluster (Fig. 17a), it is possible the relatively strong correlation arises from TCs in the non-RI group and does not extend to RI cases.

Previous studies have demonstrated EFC displays some covariance with the magnitude of vertical wind shear. The findings of DeMaria et al. (1993) and Peirano et al. (2016) determined EFC exhibits a small, but statistically significant, relationship to TC intensity change once the influence of vertical wind shear on TC intensity change is controlled for. To further quantify the relationship between EFC and TC intensity change, a multiple linear regression analysis, similar to Peirano et al. (2016), was performed for the high-PV TCs within the current dataset. Here, both EFC and the vertical wind shear magnitude were treated as independent variables in the multiple linear regression analysis. Table 5 lists the partial correlation coefficients between 24-h TC intensity change and EFC magnitude at $t = 0$ h. The partial correlation coefficients increase for TCs in the NW and NE trough clusters, as well as high-PV TCs in general, but slightly decrease for TCs in the cutoff cluster. Nonetheless, TCs in the cutoff cluster still display the most robust partial correlation coefficients between TC intensity change and EFC magnitude. These results emphasize the complex relationship between TC intensity change and EFC, as the sign of the correlation coefficient is not consistent in all clusters, even after accounting for the influence of vertical wind shear.

9. Conclusions

TCs that undergo RI are routinely associated with large forecast errors. TC intensity forecasts are further complicated when a TC interacts with an upper-tropospheric trough, as such environments are typically associated with unfavorable environmental conditions (e.g., Hanley et al. 2001); however, upper-tropospheric troughs can provide unique forcing for TC convection and intensification (Molinari and Vollaro 1989; Bosart et al. 2000; Fischer et al. 2017). This study sought to address the "good trough/bad trough" dilemma by investigating whether certain upper-tropospheric trough configurations are more favorable for RI than others. This study also aimed to identify whether the environmental and convective characteristics favorable for RI displayed dependencies on the upper-tropospheric trough morphology. The following list identifies the key results of this analysis:

- Similar upper-tropospheric trough morphologies were identified through the implementation of a k-means clustering algorithm in conjunction with t-distributed stochastic neighbor embedding (t-SNE), a machine-learning, dimensionality-reduction technique. Three clusters of unique upper-tropospheric trough morphologies were identified: the cutoff cluster, NW trough cluster, and NE trough cluster.
- Significantly greater rates of TC intensification were observed to occur for TCs in the cutoff cluster than the remaining two TC–trough configuration clusters. Additionally, TCs in the cutoff and NE trough clusters were nearly twice as likely to undergo RI than TCs in the NW trough cluster.
- Differences in the trough morphologies of RI and non-RI episodes in each TC–trough cluster were examined via composite analysis. As a whole, composites of RI episodes tended to be associated with upper-tropospheric troughs of shorter zonal wavelengths, especially at the base of the trough, and greater upstream TC–trough displacement. The presence of a cutoff low approximately 500–1000 km to the southwest of the TC appears to be a favorable configuration for RI, which is consistent with case studies of the RI of Hurricane Elena (1985) and Tropical Storm Danny (1985) performed by Molinari et al. (1995) and Molinari et al. (1998), respectively.
- In each trough cluster, RI episodes were found to be associated with significantly less ventilation of the TC with low-entropy environmental air. Some of the environmental conditions favorable for RI were found to depend on the TC–trough configuration cluster. Specifically, the distribution of MPI for RI episodes in the cutoff cluster was associated with relatively similar distributions as non-RI episodes in the NW and NE

trough clusters. These results indicate the *anomalous* thermodynamic environmental conditions, relative to similar TC–trough configurations, may be more important for RI than simply the observed MPI.

- For the first time, a climatological analysis of the relationship between the convective structure of TC–trough interactions and the rate of TC intensification was performed. Here, the convective normalization technique of Fischer et al. (2018) was employed. In each trough cluster, RI episodes were associated with significantly lower anomalous IR brightness temperature as well as anomalously large frozen hydrometeor content, consistent with anomalously vigorous deep convection (Wilheit 1986; Vivekanandan et al. 1991; Harnos and Nesbitt 2016), within 100–200 km of the TC center.

- This analysis did not find a robust or consistent relationship between EFC at the onset of an intensity change episode and RI. Additionally, EFC magnitudes for TCs in the cutoff cluster would not have satisfied the criteria for a TC–trough interaction imposed by previous studies (e.g., DeMaria et al. 1993; Hanley et al. 2001; Peirano et al. 2016). The findings of this analysis raise the question of whether EFC is a suitable metric to comprehensively identify TC–trough interactions, and whether changes in EFC may be a response to intensity changes caused by other means.

- TCs in environments with a nearby upper-tropospheric trough are associated with significantly weaker intensification rates and lower RI occurrence rates than TCs in environments devoid of upper-tropospheric troughs. Likewise, TCs interacting with upper-tropospheric troughs were characterized by significantly weaker convection, as diagnosed by IR and passive microwave satellite imagery.

Despite the utility of employing t-SNE in tandem with *k*-means clustering to identify three groups of upper-tropospheric trough morphologies, in reality, a range of different "flavors" of TC–trough interactions is observed. As such, the results of this study may oversimplify the upper-tropospheric trough characteristics favorable for RI. Additionally, since each 24-h TC intensity change episode in the presence of an upper-tropospheric trough was viewed as a unique entity, it is possible—if not likely—that for a given, prolonged, TC–trough interaction event, the upper-tropospheric trough morphology may fall into multiple different clusters over the lifetime of the event. Hypothetically, as a trough approaches from the northwest of the TC (resembling the NW trough cluster), a trough fracture event may initiate, with the fractured base of the trough shifting to the southwest of

the TC (resembling the cutoff cluster). Future work should identify whether certain paths through the t-SNE parameter space are preferred for RI. Such work could also incorporate TC–trough interactions in basins outside of the North Atlantic to determine whether the characteristics favorable for RI have a basin dependency.

Additional future work will explore other potential trough-induced forcings for convection, beyond the EFC analysis conducted in this study. Although not shown here, preliminary work has found RI episodes in the cutoff cluster are associated with regions of significantly greater quasigeostrophic ascent than non-RI episodes in the cutoff cluster, as diagnosed by the differential advection of vorticity by the thermal wind (e.g., Fischer et al. 2017). The relationship between the anomalously vigorous convection observed in RI episodes and a more complete form of the quasigeostrophic omega equation, such as an extension of the **Q**-vector form of quasigeostrophy to alternative balance (e.g., Davies-Jones 1991; Riemer et al. 2014), will be examined.

Other limitations of this analysis should also be noted. Although the greater convective activity associated with RI events was generally found to be consistent with more favorable environmental conditions, the relatively coarse resolution of the reanalysis used within this study prevents the examination of the specific pathways by which environmental conditions, such as vertical wind shear and dry air, affect TC convective structure. Future work will utilize high-resolution ensemble simulations of an observed RI event in the presence of an upper-tropospheric trough to glean how the environment affects the TC vortex- and convective-scale structures and, in turn, the rate of TC intensification.

REFERENCES

Alvey, G. R., III, J. Zawislak, and E. Zipser, 2015: Precipitation properties observed during tropical cyclone intensity change. *Mon. Wea. Rev.*, **143**, 4476–4492, https://doi.org/10.1175/MWR-D-15-0065.1.

Archambault, H. M., L. F. Bosart, D. Keyser, and J. M. Cordeira, 2013: A climatological analysis of the extratropical flow response to recurving western North Pacific tropical cyclones.

Mon. Wea. Rev., **141**, 2325–2346, https://doi.org/10.1175/MWR-D-12-00257.1.

——, D. Keyser, L. F. Bosart, C. A. Davis, and J. M. Cordeira, 2015: A composite perspective of the extratropical flow response to recurving western North Pacific tropical cyclones. *Mon. Wea. Rev.*, **143**, 1122–1141, https://doi.org/10.1175/MWR-D-14-00270.1.

Bister, M., and K. A. Emanuel, 2002: Low frequency variability of tropical cyclone potential intensity 1. Interannual to interdecadal variability. *J. Geophys. Res.*, **107**, 4801, https://doi.org/10.1029/2001JD000776.

Black, M. L., J. F. Gamache, F. D. Marks, C. E. Samsury, and H. E. Willoughby, 2002: Eastern Pacific Hurricanes Jimena of 1991 and Olivia of 1994: The effect of vertical shear on structure and intensity. *Mon. Wea. Rev.*, **130**, 2291–2312, https://doi.org/10.1175/1520-0493(2002)130<2291:EPHJOA>2.0.CO;2.

Bosart, L. F., W. E. Bracken, J. Molinari, C. S. Velden, and P. G. Black, 2000: Environmental influences on the rapid intensification of Hurricane Opal (1995) over the Gulf of Mexico. *Mon. Wea. Rev.*, **128**, 322–352, https://doi.org/10.1175/1520-0493(2000)128<0322:EIOTRI>2.0.CO;2.

Bracken, W. E., and L. F. Bosart, 2000: The role of synoptic-scale flow during tropical cyclogenesis over the North Atlantic Ocean. *Mon. Wea. Rev.*, **128**, 353–376, https://doi.org/10.1175/1520-0493(2000)128<0353:TROSSF>2.0.CO;2.

Bryan, G. H., 2008: On the computation of pseudoadiabatic entropy and equivalent potential temperature. *Mon. Wea. Rev.*, **136**, 5239–5245, https://doi.org/10.1175/2008MWR2593.1.

Cecil, D. J., and E. J. Zipser, 1999: Relationships between tropical cyclone intensity and satellite-based indicators of inner core convection: 85-GHz ice-scattering signature and lightning. *Mon. Wea. Rev.*, **127**, 103–123, https://doi.org/10.1175/1520-0493(1999)127<0103:RBTCIA>2.0.CO;2.

Chen, S. S., J. A. Knaff, and F. D. Marks, 2006: Effects of vertical wind shear and storm motion on tropical cyclone rainfall asymmetries deduced from TRMM. *Mon. Wea. Rev.*, **134**, 3190–3208, https://doi.org/10.1175/MWR3245.1.

Chen, X., Y. Wang, and K. Zhao, 2015: Synoptic flow patterns and large-scale characteristics associated with rapidly intensifying tropical cyclones in the South China Sea. *Mon. Wea. Rev.*, **143**, 64–87, https://doi.org/10.1175/MWR-D-13-00338.1.

Corbosiero, K. L., and J. Molinari, 2002: The effects of vertical wind shear on the distribution of convection in tropical cyclones. *Mon. Wea. Rev.*, **130**, 2110–2123, https://doi.org/10.1175/1520-0493(2002)130<2110:TEOVWS>2.0.CO;2.

——, and ——, 2003: The relationship between storm motion, vertical wind shear, and convective asymmetries in tropical cyclones. *J. Atmos. Sci.*, **60**, 366–376, https://doi.org/10.1175/1520-0469(2003)060<0366:TRBSMV>2.0.CO;2.

Davies-Jones, R., 1991: The frontogenetical forcing of secondary circulations. Part I: The duality and generalization of the Q vector. *J. Atmos. Sci.*, **48**, 497–509, https://doi.org/10.1175/1520-0469(1991)048<0497:TFFOSC>2.0.CO;2.

Dee, D. P., and Coauthors, 2011: The ERA-Interim reanalysis: Configuration and performance of the data assimilation system. *Quart. J. Roy. Meteor. Soc.*, **137**, 553–597, https://doi.org/10.1002/qj.828.

DeHart, J. C., R. A. Houze, and R. F. Rogers, 2014: Quadrant distribution of tropical cyclone inner-core kinematics in relation to environmental shear. *J. Atmos. Sci.*, **71**, 2713–2732, https://doi.org/10.1175/JAS-D-13-0298.1.

DeMaria, M., J. Kaplan, and J.-J. Baik, 1993: Upper-level eddy angular momentum fluxes and tropical cyclone intensity change.

J. Atmos. Sci., **50**, 1133–1147, https://doi.org/10.1175/1520-0469(1993)050<1133:ULEAMF>2.0.CO;2.

——, C. R. Sampson, J. A. Knaff, and K. D. Musgrave, 2014: Is tropical cyclone intensity guidance improving? *Bull. Amer. Meteor. Soc.*, **95**, 387–398, https://doi.org/10.1175/BAMS-D-12-00240.1.

Dvorak, V. F., 1975: Tropical cyclone intensity analysis and forecasting from satellite imagery. *Mon. Wea. Rev.*, **103**, 420–430, https://doi.org/10.1175/1520-0493(1975)103<0420:TCIAAF>2.0.CO;2.

Elsberry, R. L., T. D. B. Lambert, and M. A. Boothe, 2007: Accuracy of Atlantic and eastern North Pacific tropical cyclone intensity forecast guidance. *Wea. Forecasting*, **22**, 747–762, https://doi.org/10.1175/WAF1015.1.

Emanuel, K., and F. Zhang, 2016: On the predictability and error sources of tropical cyclone intensity forecasts. *J. Atmos. Sci.*, **73**, 3739–3747, https://doi.org/10.1175/JAS-D-16-0100.1.

Fischer, M. S., B. H. Tang, and K. L. Corbosiero, 2017: Assessing the influence of upper-tropospheric troughs on tropical cyclone intensification rates after genesis. *Mon. Wea. Rev.*, **145**, 1295–1313, https://doi.org/10.1175/MWR-D-16-0275.1.

——, ——, ——, and C. M. Rozoff, 2018: Normalized convective characteristics of tropical cyclone rapid intensification events in the North Atlantic and eastern North Pacific. *Mon. Wea. Rev.*, **146**, 1133–1155, https://doi.org/10.1175/MWR-D-17-0239.1.

Galarneau, T. J., C. A. Davis, and M. A. Shapiro, 2013: Intensification of Hurricane Sandy (2012) through extratropical warm core seclusion. *Mon. Wea. Rev.*, **141**, 4296–4321, https://doi.org/10.1175/MWR-D-13-00181.1.

Hanley, D., J. Molinari, and D. Keyser, 2001: A composite study of the interactions between tropical cyclones and upper-tropospheric troughs. *Mon. Wea. Rev.*, **129**, 2570–2584, https://doi.org/10.1175/1520-0493(2001)129<2570:ACSOTI>2.0.CO;2.

Harnos, D. S., and S. W. Nesbitt, 2011: Convective structure in rapidly intensifying tropical cyclones as depicted by passive microwave measurements. *Geophys. Res. Lett.*, **38**, L07805, https://doi.org/10.1029/2011GL047010.

——, and ——, 2016: Passive microwave quantification of tropical cyclone inner-core cloud populations relative to subsequent intensity change. *Mon. Wea. Rev.*, **144**, 4461–4482, https://doi.org/10.1175/MWR-D-15-0090.1.

Hart, R. E., and J. L. Evans, 2001: A climatology of the extratropical transition of Atlantic tropical cyclones. *J. Climate*, **14**, 546–564, https://doi.org/10.1175/1520-0442(2001)014<0546:ACOTET>2.0.CO;2.

Jones, S. C., 1995: The evolution of vortices in vertical shear. I: Initially barotropic vortices. *Quart. J. Roy. Meteor. Soc.*, **121**, 821–851, https://doi.org/10.1002/qj.49712152406.

Jones, T. A., and D. J. Cecil, 2006: Histogram matching of ASMR-E and TMI brightness temperatures., *14th Conf. on Satellite Meteorology and Oceanography*, Atlanta, GA, Amer. Meteor. Soc., P1.23, https://ams.confex.com/ams/Annual2006/techprogram/paper_100880.htm.

Judt, F., and S. S. Chen, 2016: Predictability and dynamics of tropical cyclone rapid intensification deduced from high-resolution stochastic ensembles. *Mon. Wea. Rev.*, **144**, 4395–4420, https://doi.org/10.1175/MWR-D-15-0413.1.

Kaplan, J., and M. DeMaria, 2003: Large-scale characteristics of rapidly intensifying tropical cyclones in the North Atlantic basin. *Wea. Forecasting*, **18**, 1093–1108, https://doi.org/10.1175/1520-0434(2003)018<1093:LCORIT>2.0.CO;2.

——, ——, and J. A. Knaff, 2010: A revised tropical cyclone rapid intensification index for the Atlantic and eastern North Pacific

basins. *Wea. Forecasting*, **25**, 220–241, https://doi.org/10.1175/2009WAF2222280.1.

——, and Coauthors, 2015: Evaluating environmental impacts on tropical cyclone rapid intensification predictability utilizing statistical models. *Wea. Forecasting*, **30**, 1374–1396, https://doi.org/10.1175/WAF-D-15-0032.1.

Kieper, M. E., and H. Jiang, 2012: Predicting tropical cyclone rapid intensification using the 37 GHz ring pattern identified from passive microwave measurements. *Geophys. Res. Lett.*, **39**, L13804, https://doi.org/10.1029/2012GL052115.

Knaff, J. A., S. P. Longmore, R. T. DeMaria, and D. A. Molenar, 2015: Improved tropical-cyclone flight-level wind estimates using routine infrared satellite reconnaissance. *J. Appl. Meteor. Climatol.*, **54**, 463–478, https://doi.org/10.1175/JAMC-D-14-0112.1.

Knapp, K. R., and Coauthors, 2011: Globally gridded satellite observations for climate studies. *Bull. Amer. Meteor. Soc.*, **92**, 893–907, https://doi.org/10.1175/2011BAMS3039.1.

Komaromi, W. A., and J. D. Doyle, 2018: On the dynamics of tropical cyclone and trough interactions. *J. Atmos. Sci.*, **75**, 2687–2709, https://doi.org/10.1175/JAS-D-17-0272.1.

Kossin, J. P., J. A. Knaff, H. I. Berger, D. C. Herndon, T. A. Cram, C. S. Velden, R. J. Murnane, and J. D. Hawkins, 2007: Estimating hurricane wind structure in the absence of aircraft reconnaissance. *Wea. Forecasting*, **22**, 89–101, https://doi.org/10.1175/WAF985.1.

Landsea, C. W., and J. L. Franklin, 2013: Atlantic hurricane database uncertainty and presentation of a new database format. *Mon. Wea. Rev.*, **141**, 3576–3592, https://doi.org/10.1175/MWR-D-12-00254.1.

Leroux, M.-D., M. Plu, D. Barbary, F. Roux, and P. Arbogast, 2013: Dynamical and physical processes leading to tropical cyclone intensification under upper-level trough forcing. *J. Atmos. Sci.*, **70**, 2547–2565, https://doi.org/10.1175/JAS-D-12-0293.1.

——, ——, and F. Roux, 2016: On the sensitivity of tropical cyclone intensification under upper-level trough forcing. *Mon. Wea. Rev.*, **144**, 1179–1202, https://doi.org/10.1175/MWR-D-15-0224.1.

Lin, N., R. Jing, Y. Wang, E. Yonekura, J. Fan, and L. Xue, 2017: A statistical investigation of the dependence of tropical cyclone intensity change on the surrounding environment. *Mon. Wea. Rev.*, **145**, 2813–2831, https://doi.org/10.1175/MWR-D-16-0368.1.

Maaten, L. D., 2014: Accelerating t-SNE using tree-based algorithms. *J. Mach. Learn. Res.*, **15**, 3221–3245.

——, and G. Hinton, 2008: Visualizing data using t-SNE. *J. Mach. Learn. Res.*, **9**, 2579–2605.

Mnih, V., and Coauthors, 2015: Human-level control through deep reinforcement learning. *Nature*, **518**, 529–533, https://doi.org/10.1038/nature14236.

Molinari, J., and D. Vollaro, 1989: External influences on hurricane intensity. Part I: Outflow layer eddy angular momentum fluxes. *J. Atmos. Sci.*, **46**, 1093–1105, https://doi.org/10.1175/1520-0469(1989)046<1093:EIOHIP>2.0.CO;2.

——, and ——, 1990: External influences on hurricane intensity. Part II: Vertical structure and response of the hurricane vortex. *J. Atmos. Sci.*, **47**, 1902–1918, https://doi.org/10.1175/1520-0469(1990)047<1902:EIOHIP>2.0.CO;2.

——, S. Skubis, and D. Vollaro, 1995: External influences on hurricane intensity. Part III: Potential vorticity structure. *J. Atmos. Sci.*, **52**, 3593–3606, https://doi.org/10.1175/1520-0469(1995)052<3593:EIOHIP>2.0.CO;2.

——, ——, ——, F. Alsheimer, and H. E. Willoughby, 1998: Potential vorticity analysis of tropical cyclone intensification.

J. Atmos. Sci., **55**, 2632–2644, https://doi.org/10.1175/1520-0469(1998)055<2632:PVAOTC>2.0.CO;2.

Nolan, D. S., and L. D. Grasso, 2003: Nonhydrostatic, three-dimensional perturbations to balanced, hurricane-like vortices. Part II: Symmetric response and nonlinear simulations. *J. Atmos. Sci.*, **60**, 2717–2745, https://doi.org/10.1175/1520-0469(2003)060<2717:NTPTBH>2.0.CO;2.

——, Y. Moon, and D. P. Stern, 2007: Tropical cyclone intensification from asymmetric convection: Energetics and efficiency. *J. Atmos. Sci.*, **64**, 3377–3405, https://doi.org/10.1175/JAS3988.1.

Overland, J. E., and R. W. Preisendorfer, 1982: A significance test for principal components applied to a cyclone climatology. *Mon. Wea. Rev.*, **110**, 1–4, https://doi.org/10.1175/1520-0493(1982)110<0001:ASTFPC>2.0.CO;2.

Peirano, C. M., K. L. Corbosiero, and B. H. Tang, 2016: Revisiting trough interactions and tropical cyclone intensity change. *Geophys. Res. Lett.*, **43**, 5509–5515, https://doi.org/10.1002/2016GL069040.

——, ——, and ——, 2018: Tropical cyclone intensity change under the influence of upper-level troughs in idealized simulations. *33rd Conf. on Hurricanes and Tropical Meteorology*, Ponte Vedra, FL, Amer. Meteor. Soc., 2D.1, https://ams.confex.com/ams/33HURRICANE/webprogram/Paper339352.html.

Pfeffer, R. L., and M. Challa, 1981: A numerical study of the role of eddy fluxes of momentum in the development of Atlantic hurricanes. *J. Atmos. Sci.*, **38**, 2393–2398, https://doi.org/10.1175/1520-0469(1981)038<2393:ANSOTR>2.0.CO;2.

Pielke, R. A., 2007: Future economic damage from tropical cyclones: Sensitivities to societal and climate changes. *Philos. Trans. Roy. Soc. London*, **365A**, 2717–2729, https://doi.org/10.1098/rsta.2007.2086.

Postel, G. A., and M. H. Hitchman, 1999: A climatology of Rossby wave breaking along the subtropical tropopause. *J. Atmos. Sci.*, **56**, 359–373, https://doi.org/10.1175/1520-0469(1999)056<0359:ACORWB>2.0.CO;2.

Racah, E., C. Beckham, T. Maharaj, S. Ebrahimi Kahou, M. Prabhat, and C. Pal, 2017: ExtremeWeather: A large-scale climate dataset for semi-supervised detection, localization, and understanding of extreme weather events. *Advances in Neural Information Processing Systems 30*, I. Guyon et al., Eds., Curran Associates, Inc., 3402–3413.

Rappaport, E. N., J.-G. Jiing, C. W. Landsea, S. T. Murillo, and J. L. Franklin, 2012: The Joint Hurricane Test Bed: Its first decade of tropical cyclone research-to-operations activities reviewed. *Bull. Amer. Meteor. Soc.*, **93**, 371–380, https://doi.org/10.1175/BAMS-D-11-00037.1.

Reasor, P. D., R. Rogers, and S. Lorsolo, 2013: Environmental flow impacts on tropical cyclone structure diagnosed from airborne Doppler radar composites. *Mon. Wea. Rev.*, **141**, 2949–2969, https://doi.org/10.1175/MWR-D-12-00334.1.

Reid, G. C., and K. S. Gage, 1981: On the annual variation in height of the tropical tropopause. *J. Atmos. Sci.*, **38**, 1928–1938, https://doi.org/10.1175/1520-0469(1981)038<1928:OTAVIH>2.0.CO;2.

Riemer, M., M. Baumgart, and S. Eiermann, 2014: Cyclogenesis downstream of extratropical transition analyzed by Q-vector partitioning based on flow geometry. *J. Atmos. Sci.*, **71**, 4204–4220, https://doi.org/10.1175/JAS-D-14-0023.1.

Rios-Berrios, R., and R. D. Torn, 2017: Climatological analysis of tropical cyclone intensity changes under moderate vertical wind shear. *Mon. Wea. Rev.*, **145**, 1717–1738, https://doi.org/10.1175/MWR-D-16-0350.1.

——, C. A. Davis, and R. D. Torn, 2018: A hypothesis for the intensification of tropical cyclones under moderate vertical wind

shear. *J. Atmos. Sci.*, **75**, 4149–4173, https://doi.org/10.1175/JAS-D-18-0070.1.

Rodgers, E. B., S. W. Chang, J. Stout, J. Steranka, and J.-J. Shi, 1991: Satellite observations of variations in tropical cyclone convection caused by upper-tropospheric troughs. *J. Appl. Meteor.*, **30**, 1163–1184, https://doi.org/10.1175/1520-0450(1991)030<1163:SOOVIT>2.0.CO;2.

Rogers, R., P. Reasor, and S. Lorsolo, 2013: Airborne Doppler observations of the inner-core structural differences between intensifying and steady-state tropical cyclones. *Mon. Wea. Rev.*, **141**, 2970–2991, https://doi.org/10.1175/MWR-D-12-00357.1.

Rousseeuw, P. J., 1987: Silhouettes: A graphical aid to the interpretation and validation of cluster analysis. *J. Comput. Appl. Math.*, **20**, 53–65, https://doi.org/10.1016/0377-0427(87)90125-7.

Rozoff, C. M., and J. P. Kossin, 2011: New probabilistic forecast models for the prediction of tropical cyclone rapid intensification. *Wea. Forecasting*, **26**, 677–689, https://doi.org/10.1175/WAF-D-10-05059.1.

——, C. S. Velden, J. Kaplan, J. P. Kossin, and A. J. Wimmers, 2015: Improvements in the probabilistic prediction of tropical cyclone rapid intensification with passive microwave observations. *Wea. Forecasting*, **30**, 1016–1038, https://doi.org/10.1175/WAF-D-14-00109.1.

Sampson, C. R., J. Kaplan, J. A. Knaff, M. DeMaria, and C. A. Sisko, 2011: A deterministic rapid intensification aid. *Wea. Forecasting*, **26**, 579–585, https://doi.org/10.1175/WAF-D-10-05010.1.

Shi, J. J., S. Chang, and S. Raman, 1997: Interaction between Hurricane Florence (1988) and an upper-tropospheric westerly trough. *J. Atmos. Sci.*, **54**, 1231–1247, https://doi.org/10.1175/1520-0469(1997)054<1231:IBHFAA>2.0.CO;2.

Shieh, O. H., M. Fiorino, M. E. Kucas, and B. Wang, 2013: Extreme rapid intensification of Typhoon Vicente (2012) in the South China Sea. *Wea. Forecasting*, **28**, 1578–1587, https://doi.org/10.1175/WAF-D-13-00076.1.

Tang, B., and K. Emanuel, 2012: A ventilation index for tropical cyclones. *Bull. Amer. Meteor. Soc.*, **93**, 1901–1912, https://doi.org/10.1175/BAMS-D-11-00165.1.

Tao, C., and H. Jiang, 2015: Distributions of shallow to very deep precipitation—Convection in rapidly intensifying tropical cyclones. *J. Climate*, **28**, 8791–8824, https://doi.org/10.1175/JCLI-D-14-00448.1.

——, ——, and J. Zawislak, 2017: The relative importance of stratiform and convective rainfall in rapidly intensifying tropical cyclones. *Mon. Wea. Rev.*, **145**, 795–809, https://doi.org/10.1175/MWR-D-16-0316.1.

Thorncroft, C. D., B. J. Hoskins, and M. E. McIntyre, 1993: Two paradigms of baroclinic-wave life-cycle behaviour. *Quart. J. Roy. Meteor. Soc.*, **119**, 17–55, https://doi.org/10.1002/qj.49711950903.

Velden, C., and Coauthors, 2006: The Dvorak tropical cyclone intensity estimation technique: A satellite-based method that has endured for over 30 years. *Bull. Amer. Meteor. Soc.*, **87**, 1195–1210, https://doi.org/10.1175/BAMS-87-9-1195.

Vivekanandan, J., J. Turk, and V. N. Bringi, 1991: Ice water path estimation and characterization using passive microwave radiometry. *J. Appl. Meteor.*, **30**, 1407–1421, https://doi.org/10.1175/1520-0450(1991)030<1407:IWPEAC>2.0.CO;2.

Wernli, H., and M. Sprenger, 2007: Identification and ERA-15 climatology of potential vorticity streamers and cutoffs near the extratropical tropopause. *J. Atmos. Sci.*, **64**, 1569–1586, https://doi.org/10.1175/JAS3912.1.

Wilheit, T. T., 1986: Some comments on passive microwave measurement of rain. *Bull. Amer. Meteor. Soc.*, **67**, 1226–1232, https://doi.org/10.1175/1520-0477(1986)067<1226:SCOPMM>2.0.CO;2.

Wilks, D., 2011: *Statistical Methods in the Atmospheric Sciences*. 3rd ed. International Geophysics Series, Vol. 100, Academic Press, 704 pp.

Wilson, N., and Coauthors, 2015: Combined single-cell functional and gene expression analysis resolves heterogeneity within stem cell populations. *Cell Stem Cell*, **16**, 712–724, https://doi.org/10.1016/j.stem.2015.04.004.

Zagrodnik, J. P., and H. Jiang, 2014: Rainfall, convection, and latent heating distributions in rapidly intensifying tropical cyclones. *J. Atmos. Sci.*, **71**, 2789–2809, https://doi.org/10.1175/JAS-D-13-0314.1.

Zhang, F., and D. Tao, 2013: Effects of vertical wind shear on the predictability of tropical cyclones. *J. Atmos. Sci.*, **70**, 975–983, https://doi.org/10.1175/JAS-D-12-0133.1.

Zhang, G., Z. Wang, T. J. Dunkerton, M. S. Peng, and G. Magnusdottir, 2016: Extratropical impacts on Atlantic tropical cyclone activity. *J. Atmos. Sci.*, **73**, 1401–1418, https://doi.org/10.1175/JAS-D-15-0154.1.